

# Global simulations of ice nucleation and ice supersaturation with an improved cloud scheme in the Community Atmosphere Model

A. Gettelman,<sup>1</sup> X. Liu,<sup>2</sup> S. J. Ghan,<sup>2</sup> H. Morrison,<sup>1</sup> S. Park,<sup>1</sup> A. J. Conley,<sup>1</sup> S. A. Klein,<sup>3</sup> J. Boyle,<sup>3</sup> D. L. Mitchell,<sup>4</sup> and J.-L. F. Li<sup>5</sup>

Received 31 December 2009; revised 12 May 2010; accepted 3 June 2010; published 28 September 2010.

[1] A process-based treatment of ice supersaturation and ice nucleation is implemented in the National Center for Atmospheric Research Community Atmosphere Model (CAM). The new scheme is designed to allow (1) supersaturation with respect to ice, (2) ice nucleation by aerosol particles, and (3) ice cloud cover consistent with ice microphysics. The scheme is implemented with a two-moment microphysics code and is used to evaluate ice cloud nucleation mechanisms and supersaturation in CAM. The new model is able to reproduce field observations of ice mass and mixed phase cloud occurrence better than previous versions. The model is able to reproduce observed patterns and frequency of ice supersaturation. Simulations indicate homogeneous freezing of sulfate and heterogeneous freezing on dust are both important ice nucleation mechanisms, in different regions. Simulated cloud forcing and climate is sensitive to different formulations of the ice microphysics. Arctic surface radiative fluxes are sensitive to the parameterization of ice clouds. These results indicate that ice clouds are potentially an important part of understanding cloud forcing and potential cloud feedbacks, particularly in the Arctic.

**Citation:** Gettelman, A., X. Liu, S. J. Ghan, H. Morrison, S. Park, A. J. Conley, S. A. Klein, J. Boyle, D. L. Mitchell, and J.-L. F. Li (2010), Global simulations of ice nucleation and ice supersaturation with an improved cloud scheme in the Community Atmosphere Model, *J. Geophys. Res.*, 115, D18216, doi:10.1029/2009JD013797.

## 1. Introduction

[2] Ice clouds are an important part of the climate system, and yet are poorly understood and represented in General Circulation Models (GCMs) used to simulate climate [Waliser *et al.*, 2009]. A high degree of uncertainty remains in observations of even bulk ice properties [Waliser *et al.*, 2009; Wu *et al.*, 2009]. Ice clouds have important radiative consequences in the upper troposphere [Corti *et al.*, 2005], and for regulating stratospheric humidity [Gettelman *et al.*, 2002]. Mixed phase and ice clouds are also an important part of understanding the surface radiative budget at high latitudes, and the complex interaction of clouds, radiation and surface properties play a role in regulating Arctic sea ice and Arctic climate [Kay and Gettelman, 2009]. Despite the importance of ice clouds to climate, there are still large uncertainties in our theoretical understanding of ice cloud processes [Prenni *et al.*, 2007], such as ice nucleation, growth

and aggregation. In part, these uncertainties stem from measurement uncertainties, due to the difficulty of observing ice in clouds from space or in situ aircraft.

[3] There are wide discrepancies in observations of ice crystal numbers. [Gayet *et al.*, 2004] reported median cirrus cloud ice crystal numbers of  $1000\text{--}3000 \text{ L}^{-1}$  from the interhemispheric difference in cirrus properties from anthropogenic emissions (INCA) experiment. Jensen *et al.* [2009] recently reported ice crystal numbers of  $100 \text{ L}^{-1}$  or less in tropical cirrus clouds and aged anvils during the Tropical Composition, Cloud and Climate Coupling (TC4) campaign. As noted by Heymsfield [2007] and McFarquhar *et al.* [2007a] there is now compelling evidence that because of crystal shattering on probes, in situ measurements of ice crystals may have overestimated number concentrations by a factor of four [Field *et al.*, 2007] or even 1–2 orders of magnitude [Jensen *et al.*, 2009]. The values reported by Jensen *et al.* [2009] used probes with an open path design less subject to shattering.

[4] Nucleation of ice crystals is a process very distinct from liquid condensation. Ice nucleation requires either a liquid drop to freeze (homogeneous freezing) and/or a crystal to begin forming or freezing on a nucleus (heterogeneous nucleation). The relative scarcity of ice nuclei, and the higher nucleation thresholds for those that exist, lead to much higher saturation over ice than over water in the atmosphere [Gettelman *et al.*, 2006a]. Heterogeneous nucleation may

<sup>1</sup>Atmospheric Chemistry Division, National Center for Atmospheric Research, Boulder, Colorado, USA.

<sup>2</sup>Pacific Northwest National Laboratory, Richland, Washington, USA.

<sup>3</sup>Lawrence Livermore National Laboratory, Livermore, California, USA.

<sup>4</sup>Desert Research Institute, Reno, Nevada, USA.

<sup>5</sup>Jet Propulsion Laboratory, Pasadena, California, USA.

**Table 1.** Predicted Species for Interstitial and Cloud-Borne Component of Each Aerosol Mode<sup>a</sup>

Aitken Mode	Accumulation Mode	Coarse Mode
Number mixing ratio	number mixing ratio	number mixing ratio
Sulfate mmr	sulfate mmr	sulfate mmr
Sea salt mmr	sea salt mmr	sea salt mmr
Secondary organic mmr	secondary organic mmr black carbon mmr soil dust mmr primary organic mmr	soil dust mmr

<sup>a</sup>Here mmr, mass mixing ratio.

significantly lower the threshold supersaturation required for ice nucleation, with significant impacts on the microphysical and macrophysical evolution of clouds [Kärcher et al., 2007].

[5] Many GCM parameterizations of stratiform cloud formation do not permit ice supersaturation in pure ice clouds and fix ice mass fraction of total condensed water (ice mass divided by ice and liquid mass) as a function of temperature [Roeckner et al., 1996; DelGenio et al., 1996; Zhang et al., 2003]. Rotstayn et al. [2000] developed a parameterization for estimating the ice fraction in global models using a physically based treatment of vapor deposition. Recently, several schemes have been developed that either parameterize ice supersaturation for ice nucleation [Kärcher et al., 2006; Kärcher and Burkhardt, 2008] or explicitly allow ice supersaturation [Liu et al., 2007; Storelvmo et al., 2008]. Lohmann et al. [2007] relaxed saturation adjustment for cirrus clouds in the ECHAM5 GCM. Ice supersaturation in global models [Tompkins et al., 2007; Gettelman and Kinnison, 2007] has been shown to affect clouds, radiation and the transport of ozone and water vapor into the stratosphere.

[6] Here, we combine theoretical elements of previous work to extend the treatment of ice nucleation described by Liu et al. [2007] in the National Center for Atmospheric Research (NCAR) Community Atmosphere Model (CAM). The new scheme works with a new cloud microphysical, macrophysical and aerosol scheme. It integrates a new microphysical scheme with the Liu et al. [2007] ice nucleation code, as well as a new description of vapor deposition in the mixed phase. The scheme is evaluated against a suite of in situ and satellite observations using climatologies and assimilation techniques.

[7] We describe the scheme and sensitivity, and explore the effect of different assumptions about ice microphysics on climate. Section 2 will describe the new scheme, section 3 presents detailed results and comparisons to observations. Sensitivity of the solutions to key parameters is described in section 4, and the climate impact of the scheme is detailed in section 5. Conclusions are given in section 6.

## 2. Scheme Description

[8] We start with the National Center for Atmospheric Research (NCAR) Community Atmosphere Model (CAM), version 3 [Collins et al., 2004, 2006]. To this base model, several important changes are added. The deep convection scheme closure has been modified following Neale et al. [2008]. The moist boundary layer scheme is described by

Bretherton and Park [2009], and the shallow cumulus convection scheme is that of Park and Bretherton [2009]. The updated model uses the implementation of a new 4 class (liquid, ice, rain and snow), two-moment stratiform cloud microphysics scheme described by Morrison and Gettelman [2008] (hereafter MG2008) and implemented as described in Gettelman et al. [2008]. The model radiation code has been updated to the Rapid Radiative Transfer Model for GCMs (RRTMG) described by Iacono et al. [2008], and a new radiation interface developed for the MG2008 micro-physics. The liquid cloud macrophysical closure is described by S. Park et al. (manuscript in preparation, 2010).

[9] The aerosol treatment in the model uses a modal based scheme similar to that described by Easter et al. [2004], but with only three modes (Aitken, accumulation, and coarse). The predicted internally mixed aerosol species for each log-normal mode are listed in Table 1. Ammonium is diagnosed from sulfate assuming sulfate is partially neutralized by in the form of  $\text{NH}_4\text{H}_2\text{SO}_4$ . Liu et al. (Toward a Minimal Representation of Aerosol Direct and Indirect Effects, in preparation, 2010) show that this scheme yields results very similar to a more complete seven-mode scheme that predicts ammonia and includes separate modes for primary carbonaceous aerosol and coarse and fine sea salt and soil dust.

[10] From this base case, we modify further the mixed phase and ice phase of the model as detailed below. We modify (1) the [Slingo, 1987] fractional cloudiness scheme for the ice phase, (2) the macrophysical (bulk condensation) closure assumptions for ice, (3) the treatment of the mixed phase, (4) ice nucleation and ice process rates in the MG2008 microphysics scheme, and (5) the radiative effects of ice. The scheme provides improved physics for ice, including ice supersaturation and ice cloud-aerosol interactions through ice crystal nucleation pathways.

### 2.1. Cloud Fraction

[11] Several modifications have been made to the determination of diagnostic fractional cloudiness in the simulations. The ice and liquid cloud fractions are now calculated separately. Ice and liquid cloud can exist in the same grid box. Total cloud fraction, used for radiative transfer, is determined assuming maximum overlap between the two.

[12] The diagnostic ice cloud fraction closure is constructed using a total water formulation of the [Slingo, 1987] scheme. There is an indirect dependence of prognostic cloud ice on the ice cloud fraction since the in-cloud ice content is used for vapor deposition. The new formulation of ice cloud fraction ( $CF_i$ ) is calculated using relative humidity (RH) based on total ice water mixing ratio, including the ice mass mixing ratio ( $q_i$ ) and the vapor mixing ratio ( $q_v$ ). The RH based on total ice water ( $RH_{ti}$ ) is then  $RH_{ti} = (q_v + q_i)/q_{sat}$  where  $q_{sat}$  is the saturation vapor mixing ratio over ice. Because this is for ice clouds only, we do not include  $q_l$  (liquid mixing ratio). We have tested that the inclusion of  $q_l$  does not substantially impact the scheme (since there is little liquid present in this regime).

[13] Ice cloud fraction is then given by  $CF_i = \min(1, RH_d^2)$  where

$$RH_d = \max\left(0, \frac{RH_{ti} - RH_{i\min}}{RH_{i\max} - RH_{i\min}}\right) \quad (1)$$

$RHi_{\max}$  and  $RHi_{\min}$  are prescribed maximum and minimum threshold humidities with respect to ice, set at  $RHi_{\max} = 1.1$  and  $RHi_{\min} = 0.8$ . These are adjustable parameters that reflect assumptions about the variance of humidity in a grid box. The scheme is not very sensitive to  $RHi_{\min}$ .  $RHi_{\max}$  affects the total ice supersaturation and ice cloud fraction.

[14] With  $RHi_{\max} = 1$  and  $q_i = 0$  the scheme reduces to the [Slingo, 1987] scheme.  $RH_{ti}$  is preferred over  $RH$  in  $RH_d$  because when  $q_i$  increases due to vapor deposition, it reduces  $q_v$ , and without any precipitation or sedimentation the decrease in RH would change diagnostic cloud fraction, whereas  $RH_{ti}$  is constant.

[15] An alternative closure is examined in section 4 below.

## 2.2. Cloud Macrophysics Closure

[16] The closure assumptions of S. Park et al. (manuscript in preparation, 2010) have been modified to perform bulk saturation adjustment only on water saturation. This permits supersaturation over ice for ice and mixed phase clouds. Large-scale condensation occurs with respect to ice (deposition) only when ice is present, and is calculated with process rates for vapor deposition onto the ice. Whole grid saturation occurs when the RH with respect to liquid water ( $RH_w$ ) is greater than 1. Partial grid saturation occurs for liquid when  $RH_w$  is greater than a critical RH ( $RH_{crit}$ ). The details of the formulation to define a liquid cloud fraction and bulk liquid condensation are described by S. Park et al. (manuscript in preparation, 2010).

[17] Evaporation occurs if the air is subsaturated with respect to water for liquid, and sublimation occurs when air is subsaturated with respect to ice. Excess supersaturation is removed only with respect to water, not ice.

## 2.3. Cloud Microphysics

[18] In addition to the macrophysics changes and modifications to treatment of supersaturation, we also modify treatment of vapor deposition onto ice and the Bergeron-Findeisen process. In mixed phase clouds, the treatment of vapor deposition and the Bergeron-Findeisen process is similar to MG08 and Rotstayn et al. [2000]. Condensate formed within the time step by grid-scale processes (e.g., radiative cooling, large-scale ascent, etc.) via the macrophysical condensation closure (see section 2.2) is assumed to be initially liquid. Vapor deposition onto ice occurs if ice is present and the temperature is below freezing, and is calculated assuming that the in-cloud water vapor mixing ratio is saturated with respect to liquid water (see equations (21)–(22) in MG08). Vapor deposition in mixed phase clouds depletes part or all of the liquid condensate. Note that in the current implementation we assume maximum overlap between the liquid and ice cloud cover fractions. This is similar to the “uniformly mixed” assumption discussed in Rotstayn et al. [2000], in contrast to minimum overlap which is similar to the “horizontally adjacent” assumption discussed by Rotstayn et al. [2000, Figure 2]. The scheme described here could be easily modified for any overlap assumption. The assumption of maximum (minimum) overlap implies the largest (smallest) possible depletion rate of liquid water via the Bergeron-Findeisen process. In situ observations reveal

the close proximity of liquid and ice particles in mixed phase clouds, but also suggest that for spatial scales of order 100 m and less, mixed phase clouds tend to be composed of either mostly ice or liquid in terms of mass [Korolev et al., 2003].

[19] Several cases are treated below that involve ice deposition in ice-only clouds or mixed phase clouds in which all liquid water is depleted within the time step. Case [1]: Ice only clouds in which  $q_v > q_{vi}^*$  where  $q_v$  is the grid mean water vapor mixing ratio and  $q_{vi}^*$  is the local vapor mixing ratio at ice saturation ( $q_{sat}$ ). Case [2] is the same as case [1] ( $q_v > q_{vi}^*$ ) but there is existing liquid water depleted by the Bergeron-Findeisen process (ber). Case [3]: Liquid water is depleted by the Bergeron-Findeisen process and the local liquid is less than local ice saturation ( $q_v^* \leq q_{vi}^*$ ). In Case [4]  $q_v < q_{vi}^*$  so sublimation of ice occurs.

[20] Case [1]: If the ice cloud fraction is larger than the liquid cloud fraction (including grid cells with ice but no liquid water), or if all new and existing liquid water in mixed phase clouds is depleted via the Bergeron-Findeisen process within the time step, then vapor depositional ice growth occurs at the expense of water vapor. In the case of a grid cell where ice cloud fraction exceeds liquid cloud fraction, vapor deposition in the pure ice cloud portion of the cell is calculated similarly to equation (21) in MG08:

$$\left(\frac{\partial q_i}{\partial t}\right)_{dep} = \frac{(q_v - q_{vi}^*)}{\Gamma_p \tau}, q_v > q_{vi}^* \quad (2)$$

where  $\Gamma_p = 1 + \frac{L_s}{c_p} \frac{dq_{vi}}{dT}$  is the psychrometric correction to account for the release of latent heat,  $L_s$  is the latent heat of sublimation,  $c_p$  is the specific heat at constant pressure,  $\frac{dq_{vi}}{dT}$  is the change of ice saturation vapor pressure with temperature, and  $\tau$  is the supersaturation relaxation timescale associated with ice deposition given by equation (22) in MG08 (a function of ice crystal surface area and the diffusivity of water vapor in air). The assumption for pure ice clouds is that the in-cloud vapor mixing ratio for deposition is equal to the grid-mean value. The same assumption is used in Liu et al. [2007], and while it is uncertain, it is the most straightforward. Thus we do not consider subgrid variability of water vapor for calculating vapor deposition in pure ice clouds.

[21] The form of the deposition rate in equation (2) differs from that used by Rotstayn et al. [2000] and Liu et al. [2007] because they considered the increase in ice mixing ratio  $q_i$  due to vapor deposition during the time step, and formulated an implicit solution based on this consideration (see equation (6) in Rotstayn et al. [2000]). However, these studies did not consider sinks for the ice due to processes such as sedimentation and conversion to precipitation when formulating their implicit solution; these sink terms may partially (or completely) balance the source for the ice due to vapor deposition. Thus, we use a simple explicit forward-in-time solution that does not consider changes of  $q_i$  within the microphysics time step.

[22] Case [2]: When all new and existing liquid water is depleted via the Bergeron-Findeisen process (ber) within the time step, the vapor deposition rate is given by a weighted average of the values for growth in mixed phase conditions prior to the depletion of liquid water (first term on the right

hand side) and in pure ice clouds after depletion (second term on the right hand side):

$$\left( \frac{\partial q_i}{\partial t} \right)_{dep} = \frac{q_c^*}{\Delta t} + \left( 1 - \frac{q_c^*}{\Delta t} \left( \frac{\partial q_i}{\partial t} \right)_{ber}^{-1} \right) \left( \frac{(q_v^* - q_{vi}^*)}{\Gamma_p \tau} \right), q_v > q_{vi}^* \quad (3)$$

where  $q_c^*$  is the sum of existing and new liquid condensate mixing ratio,  $\Delta t$  is the model time step,  $(\frac{\partial q_i}{\partial t})_{ber}$  is the ice deposition rate in the presence of liquid water (i.e., assuming vapor mixing ratio is equal to the value at liquid saturation) as described above, and  $q_v^*$  is an average of the grid-mean vapor mixing ratio and the value at liquid saturation.

[23] Case [3]: If  $q_v^* \leq q_{vi}^*$  then it is assumed that no additional ice deposition occurs after depletion of the liquid water. The deposition rate in this instance is given by:

$$\left( \frac{\partial q_i}{\partial t} \right)_{dep} = \left( \frac{q_c^*}{\Delta t} \right), q_v^* \leq q_{vi}^* \quad (4)$$

[24] Case [4]: Sublimation of pure ice cloud occurs when the grid-mean water vapor mixing ratio is less than value at ice saturation. In this case the sublimation rate of ice is given by:

$$\left( \frac{\partial q_i}{\partial t} \right)_{sub} = \frac{(q_v - q_{vi}^*)}{\Gamma_p \tau}, q_v < q_{vi}^* \quad (5)$$

Again, the use of grid-mean vapor mixing ratio in equation (5) follows the assumption of Liu et al. [2007] that the in-cloud  $q_v$  is equal to the grid box mean in pure ice clouds. Grid-mean deposition and sublimation rates are given by the in-cloud values for pure ice or mixed phase clouds described above, multiplied by the appropriate ice or mixed phase cloud fraction. Finally, ice deposition and sublimation are limited to prevent the grid-mean mixing ratio from falling below the value for ice saturation in the case of deposition and above this value in the case of sublimation.

## 2.4. Ice Initiation

[25] Ice crystal nucleation is based on Liu et al. [2007], which includes homogeneous freezing of sulfate competing with heterogeneous immersion freezing on mineral dust in ice clouds (with temperatures below  $-37^\circ\text{C}$ ) [Liu and Penner, 2005]. Because mineral dust at cirrus levels is very likely coated [Wiacek and Peter, 2009], deposition nucleation is not explicitly included in this work for pure ice clouds. Immersion freezing is treated for cirrus (pure ice), but not for mixed phase clouds. The relative efficiency of immersion versus deposition nucleation in mixed phase clouds is an unsettled problem, and the omission of immersion freezing in mixed phase clouds may not be appropriate (but is implicitly included in the deposition/condensation nucleation: see below). Deposition nucleation may act at temperatures lower than immersion nucleation (i.e.,  $T < -25^\circ\text{C}$ ) [Field et al., 2006], and immersion nucleation has been inferred to dominate in mixed phase clouds [Ansmann et al., 2008, 2009; Hoose and Kristjansson, 2010]. We have

not treated immersion freezing on soot because while Liu and Penner [2005] assumed it was an efficient mechanism for ice nucleation, more recent studies [Kärcher et al., 2007] indicate it is still highly uncertain.

[26] In the mixed phase cloud regime ( $-37 < T < 0^\circ\text{C}$ ), deposition/condensation nucleation is considered based on Meyers et al. [1992], with a constant nucleation rate for  $T < -20^\circ\text{C}$ . The Meyers et al. [1992] parameterization is assumed to treat deposition/condensation on dust in the mixed phase. Since it is based on observations taken at water saturation, it should include all important ice nucleation mechanisms (such as the immersion and deposition nucleation discussed above) except contact nucleation, though we cannot distinguish all the specific processes. Here we explore scaling it with respect to dust concentration in section 4. Meyers et al. [1992] has been shown to produce too many ice nuclei during the Mixed Phase Arctic Clouds Experiment (MPACE) by Prenni et al. [2007]. See analysis of the MPACE case in section 3. Contact nucleation by mineral dust is included based on Young [1974] and related to the coarse mode dust number. It acts in the mixed phase where liquid droplets are present and includes Brownian diffusion as well as phoretic forces. Hallet-Mossop secondary ice production due to accretion of drops by snow is included following [Cotton et al., 1986].

[27] In the Liu and Penner [2005] scheme, the number of ice crystals nucleated is a function of temperature, humidity, sulfate, dust and updraft velocity, derived from fitting the results from cloud parcel model experiments. A threshold  $RH_w$  for homogeneous nucleation was fitted as a function of temperature and updraft velocity (see Liu et al. [2007], equation 6). For driving the parameterization, the subgrid velocity for ice ( $w_{sub}$ ) is derived from the square root of the Turbulent Kinetic Energy (TKE) following [Morrison and Pinto, 2005]:

$$w_{sub} = \sqrt{\frac{2}{3} TKE} \quad (6)$$

where TKE is defined using a steady state energy balance (equation (17) and (28) in Bretherton and Park [2009]). In the baseline case a minimum of  $0.2 \text{ m s}^{-1}$  is set (see section 4 for further discussion). The overall distribution of  $w_{sub}$  is similar to observations during the INCA experiment [Kärcher and Ström, 2003]. The minimum limit is reached a significant fraction (1/3) of the time. We test the effect of this limit in section 4.

[28] It is also implicitly assumed that there is some variation in humidity over the grid box. For purposes of ice nucleation, nucleation rates for a grid box are estimated based on the ‘most humid portion’ of the grid-box. This is assumed to be the grid box average humidity plus a fixed value (20% RH). This implies that the ‘local’ threshold supersaturation for ice nucleation will be reached at a grid box mean value 20% lower than the RH process threshold value. This represents another gross assumption about the RH variability in a model grid box and is an adjustable parameter in the scheme. In the baseline case, sulfate for homogeneous freezing is taken as the portion of the Aitken mode particles with radii greater than 0.1 microns, and was chosen to better reproduce observations (this too can be adjusted to alter the balance of homogeneous freezing).

**Table 2.** CAM Cases Discussed in the Text

Case Name	Description
CNTL	no supersaturation, fixed ice nucleation
ICE	supersaturation and ice nucleation
FIXIN	supersaturation and fixed ice nucleation
ICEHI	supersaturation, ice nucleation, high ice number
Sensitivity Test	Description
DCS	reduce threshold size for ice autoconversion
NUCALL	homogeneous and heterogeneous freezing at all temperatures
WSUB	reduce subgrid vertical velocity
ICLDF	different ice cloud closure (empirical IWC)
DUST	use dust number concentration to scale deposition-condensation freezing
FRZ	freeze rain homogeneously at $-40^{\circ}\text{C}$

The size represents the large tail of the Aitken mode. In the upper troposphere there is little sulfate in the accumulation mode (it falls out), and almost all sulfate is in the Aitken mode.

## 2.5. Radiative Treatment of Ice

[29] The simulations use a self consistent treatment of ice in the radiation code. The radiation code uses as input the prognostic effective radius of ice from the cloud microphysics (MG2008, equation (5)). Ice cloud optical properties are calculated based on the modified anomalous diffraction approximation (MADA), described in *Mitchell* [2000, 2002] and *Mitchell et al.* [2006a]. The mass-weighted extinction (volume extinction coefficient/ice water content) and the single scattering albedo,  $\omega_0$ , are evaluated using a look-up table. For solar wavelengths, the asymmetry parameter  $g$  is determined as a function of wavelength and ice particle size and shape as described in *Mitchell et al.* [1996] and *Nousiainen and McFarquhar* [2004] for quasi-spherical ice crystals. For terrestrial wavelengths,  $g$  was determined following *Yang et al.* [2005]. An ice particle shape recipe was assumed when calculating these optical properties. The recipe is described in *Mitchell et al.* [2006b] based on midlatitude cirrus cloud data from *Lawson et al.* [2006] and consists of 50% quasi-spherical and 30% irregular ice particles, and 20% bullet rosettes for the cloud ice (i.e., small crystal) component of the ice particle size distribution (PSD). Snow is also included in the radiation code, using the diagnosed mass and effective radius of falling snow crystals (MG2008). For the snow component, the ice particle shape recipe was based on the crystal shape observations reported in *Lawson et al.* [2006] at  $-45^{\circ}\text{C}$ : 7% hexagonal columns, 50% bullet rosettes and 43% irregular ice particles. The radiative effects of snow are a subject of a future investigation.

## 2.6. Implementation and Numerical Aspects

[30] The scheme is implemented in CAM3 [*Collins et al.*, 2004] with the modifications described by *Gettelman et al.* [2008] and the other parameterizations above. In the time step loop, the physical parameterizations are calculated using a time split approach, whereby tendencies from each process

are added to the state variables before the next process is calculated. The stratiform cloud scheme is executed before the radiative transfer code and before coupling to the surface processes but after deep and shallow convection schemes. There are several components of the stratiform cloud scheme. First, detrained condensate from deep and shallow convection is added to cloud liquid and ice using the detrained mass with an assumed effective radius of spherical particles (8 microns for liquid and 25 microns for ice) to estimate number. A simple linear partition between liquid and ice over the range of  $-5 < T < -35^{\circ}\text{C}$  is used for detrained condensate. Then the cloud macrophysics is called to determine cloud fraction for liquid and ice and bulk net condensation or evaporation for liquid. Finally the cloud microphysics is called.

[31] Numerically, several key aspects of the scheme are limited to ensure mass conservation and reasonable values for cloud fraction, mass and number concentrations. Ice nucleation is limited by the available activated nuclei and the available vapor above saturation. Process rates are required to conserve mass and number. Number concentrations for liquid and ice are forced to be consistent with condensed mass so that number does not exist without mass and crystal diameter ( $D_i$ ) is in the range  $10 < D_i < 400 \mu\text{m}$  as in MG2008. Droplet diameter ( $D_l$ ) is in the range  $2 < D_l < 50 \mu\text{m}$ . Cloud fractions are constrained to be nonzero only when condensed mass is present and a minimum in-cloud mass threshold of  $5 \text{ mg kg}^{-1}$  for clouds is assumed (the same for liquid and ice).

## 3. Results

[32] In this section we present a series of cases that illustrate the performance of the scheme. The next section will analyze some of the detailed aspects of the scheme. The ‘ICE’ case is the basic version of the scheme. It can be compared to a control case, ‘CNTL,’ that uses saturation adjustment to a ‘hybrid’ (liquid and ice) RH dependent on temperature from  $-20 < T < 0^{\circ}\text{C}$  as in CAM3. Within this range some ice supersaturation can exist. The CNTL case also has ice nucleation fixed as a function of temperature as described in MG2008 using *Cooper* [1986]. The ‘FIXIN’ case has supersaturation, but uses ice nucleation following *Cooper* [1986] as described in MG2008. The ‘ICEHI’ case is a version of the ‘ICE’ case with higher ice nuclei and ice crystal number concentrations. Higher concentrations result from increasing the crystal number from homogeneous freezing by using all sulfate particles in the Aitken mode. These cases are summarized in Table 2.

### 3.1. CAPT Experiments

[33] To evaluate the role of the ice scheme in mixed phase clouds, we compare CAM simulations to field observations collected during the Atmospheric Radiation Measurement (ARM) program’s MPACE project [*Verlinde et al.*, 2007]. MPACE was conducted near Barrow, Alaska in October 2004 and during the experiment there was a significant mix of deep and shallow clouds, as well as a high proportion of mixed phase clouds. To compare CAM with the observations, we utilize a weather forecasting approach [*Phillips et al.*, 2004] as applied in the Cloud Associated Parameterization Testbed (CAPT) [*Xie et al.*, 2008]. Model output for the grid-box closest to Barrow is examined for the second day of forecasts that are initialized every day in October 2004 with

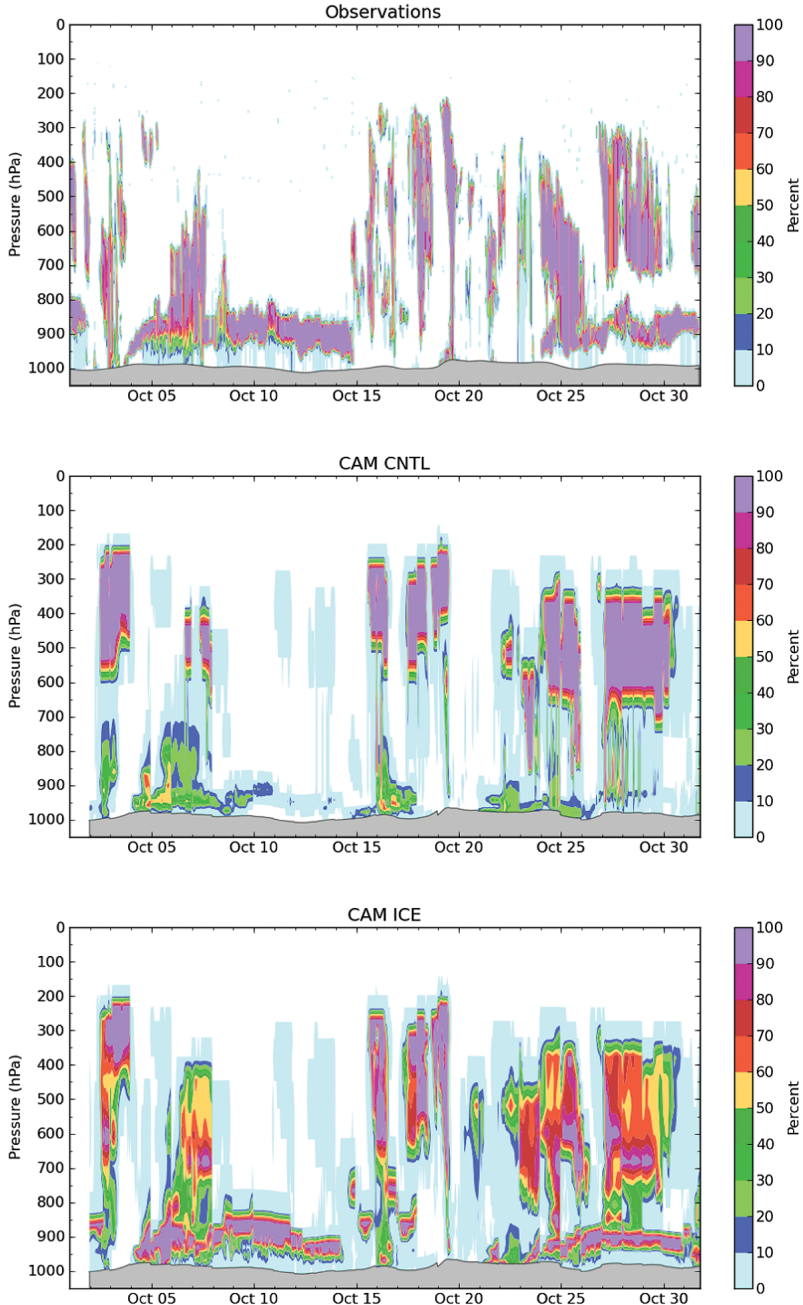


**Figure 1.** Height-time profile of cloud fraction (%) for Barrow, Alaska, during October 2004: (top) as observed from ARM cloud radars and lidars Active Remotely Sensed Cloud Locations algorithm [Clothiaux et al., 2000], (middle) CNTL simulation, and (bottom) ICE simulation. Simulations use the CAPT weather forecast approach.

reanalyses produced by the Modern Era Retrospective-Analysis for Research and Applications (MERRA) project (<http://gmao.gsfc.nasa.gov/research/merra/>).

[34] Figure 1 illustrates the hourly mean cloud fraction as a function of time and pressure from observations and model simulations. The observations (Figure 1, top) are from the Active Remotely Sensed Cloud Locations algorithm [Clothiaux et al., 2000] which uses signals from the cloud radar and lidar at Barrow. The lower two panels illustrate the model's hourly mean cloud fraction from the CNTL simulation which does not permit ice supersaturation (Figure 1,

middle) and the ICE simulation with the revised ice microphysics (Figure 1, bottom) including ice supersaturation and nucleation. The quantity from the model is not identical to that of the observations. Addressing the sources of differences between the model definition and that retrieved from upward-pointed radars and lidars is not easily done. While we don't have any expectation of bias, there are a number of difficult issues involved such as instrument sensitivity for detection of hydrometeors and differences between a point observation averaged over time (which is the observation) and an grid-box area-averaged quantity

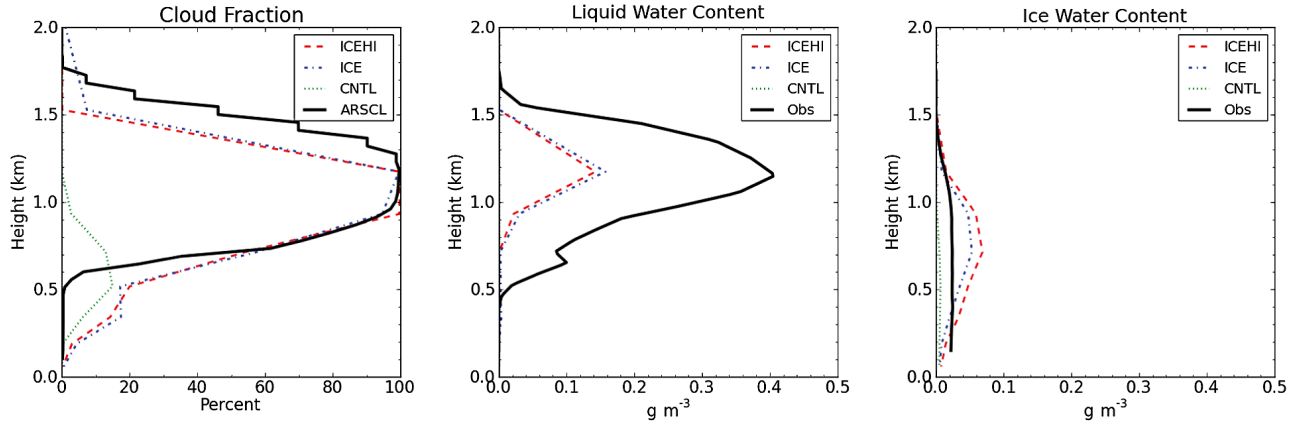


**Figure 2.** Height-profile of quantities averaged over the period 1200 UTC 9 October to 1200 UTC 10 October during MPACE. (left) Cloud fraction (%). (middle) Liquid water content. (right) Ice water content. Observations in black. Cloud fraction observations are from Active Remotely Sensed Cloud Locations (ARSCL) [Clothiaux et al., 2000]; liquid and ice water content are from Shupe et al. [2008]. Simulations for CNTL (green dash), ICE (blue dash), and ICEHI (red) shown.

from the model. But, both model versions simulate a reasonable progression of middle and high cloud in response to various frontal passages. A prominent difference is the much larger amount of boundary-layer clouds in the ICE simulation in better agreement with the observations. These boundary layer clouds were observed to be mixed phase (Figure 2) and the presence of supercooled liquid allows these clouds to be long-lived due to turbulence driven by the strong cloud-top longwave cooling that occurs only when cloud liquid is present. Surface fluxes also play a role, but are similar in these simulations. While the ICE simulation produces an appreciable amount of supercooled liquid, the CNTL simulation simulates essentially no supercooled liquid and thus simulates very low amounts of boundary-layer cloud. Perhaps the absence of supersaturation in the CNTL simulation allows more condensation and thus has depleted the available humidity. Relative to the CNTL simulation, the presence of significant amounts of supercooled liquid in the ICE simulation leads to a greatly improved simulation of the downward longwave radiation at the surface (not shown).

[35] The boundary-layer mixed phase clouds observed during 9–15 October were sampled by aircraft and have been the subject of numerous modeling studies ([Klein et al., 2009; Solomon et al., 2009], among others). Figure 2 shows the average for a 1 day (9–10 October) period of cloud fraction and liquid and Ice Water Content (IWC) from remote sensor retrievals [Shupe et al., 2008] and model simulations. Simulated IWC includes snow (precipitating ice). The ICE and ICEHI simulations correctly simulate an overcast cloud with appreciable amounts of liquid and that produces ice and snow that falls out of the cloud. However, both simulations underestimate the amount of supercooled liquid by 50% (Figure 2, middle) and overestimate the amount of ice and snow by 50% (Figure 2, right). These biases also appear when comparing model simulations relative to the aircraft retrievals [McFarquhar et al., 2007b] and during the whole of the 6 day period with mixed phase boundary-layer cloud. The biases in supercooled liquid are a common feature of many models for this case [Klein et al., 2009]. Although many factors may

contribute to this bias, it is noteworthy that the model simulates a snow crystal number concentration of nearly  $100 \text{ L}^{-1}$ . The ice crystal concentration in clouds is  $<1 \text{ L}^{-1}$ . Thus most of the ice and snow number concentration is snow. The total ice and snow concentration far exceeds the observed ice number concentration of  $2 \text{ L}^{-1}$  [McFarquhar et al., 2007b] for large crystals (and would include snow). This suggests that the model's snow production is too strong, at least for this region and time.

[36] High snow numbers are due to freezing of all supercooled rain instantaneously at temperatures less than  $-5^\circ\text{C}$ . This was included to prevent excessive supercooled rain in the Arctic spring that negatively impacts sea ice distributions. In an experiment where this freezing threshold is reduced to  $-40^\circ\text{C}$  (FRZ), total ice and snow numbers simulated by CAPT are only  $1 \text{ L}^{-1}$ . In this test the immersion freezing of some fraction of the rain mass is allowed above this temperature threshold following the formulation described in MG08. The FRZ case does improve agreement with observations for the MPACE case, but degrades general simulations because the sea ice model does not treat supercooled liquid precipitation.

### 3.2. Ice

[37] The performance of the scheme can also be evaluated by looking at the climatological (average) representation of ice number, the total mass of ice and the in-cloud ice water content compared to observations. Results are averages from 3 year runs with fixed present day sea surface temperatures and aerosol emissions after a 1 year spin up. Simulations are performed at  $1.9^\circ$  latitude by  $2.5^\circ$  longitude horizontal resolution with 30 vertical levels up to 3 hPa. Upper tropospheric vertical resolution is about 1 km and is shown as vertical ticks on Figure 4a (some ticks are omitted in the boundary layer for clarity).

[38] The ice mass mixing ratio fraction (or ice fraction, FICE) with respect to temperature is illustrated in Figure 3 following that of Korolev et al. [2003, Figure 5]. Figure 3 shows a series of probability distribution functions (PDFs) in different temperature ranges from observations (Figure 3a)

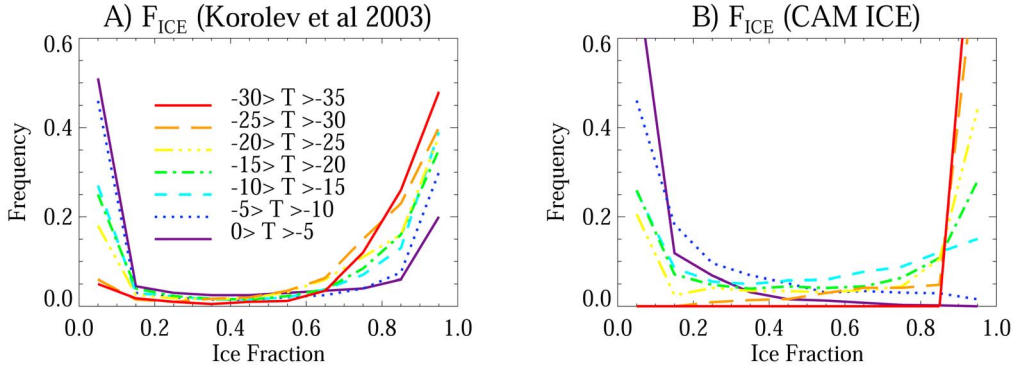


**Figure 3.** PDFs of ice mass fraction ( $F_{\text{ICE}}$ ) within given temperature ranges from (a) *Korolev et al.* [2003] and (b) CAM ICE case. Model output is from 1000 to 100 hPa and 90°S–90°N.

and from output of the ‘ICE’ case (Figure 3b). Model output is only shown for mixed phase conditions when ice and liquid are present ( $q_i$  and  $q_l > 0$ ). Ice mass fraction is calculated at each model point (1000–100 hPa and 90°S–90°N) and time, as is temperature, and then the PDFs are constructed from monthly means of each, point by point. The shape of a joint PDF of instantaneous values is similar.

[39] The transition from ice to liquid occurs between  $-2^{\circ}\text{C}$  and  $-20^{\circ}\text{C}$  in observations and  $-5^{\circ}\text{C}$  and  $-20^{\circ}\text{C}$  in the simulation. In the ICE simulation, the maximum frequency at an ice fraction of 0.6 is between  $-10^{\circ}\text{C}$  and  $-15^{\circ}\text{C}$ . There is not enough ice mass fraction (relative to the observations) at temperatures warmer than  $-15^{\circ}\text{C}$ , indicating a slightly more narrow transition temperature range in the simulations,

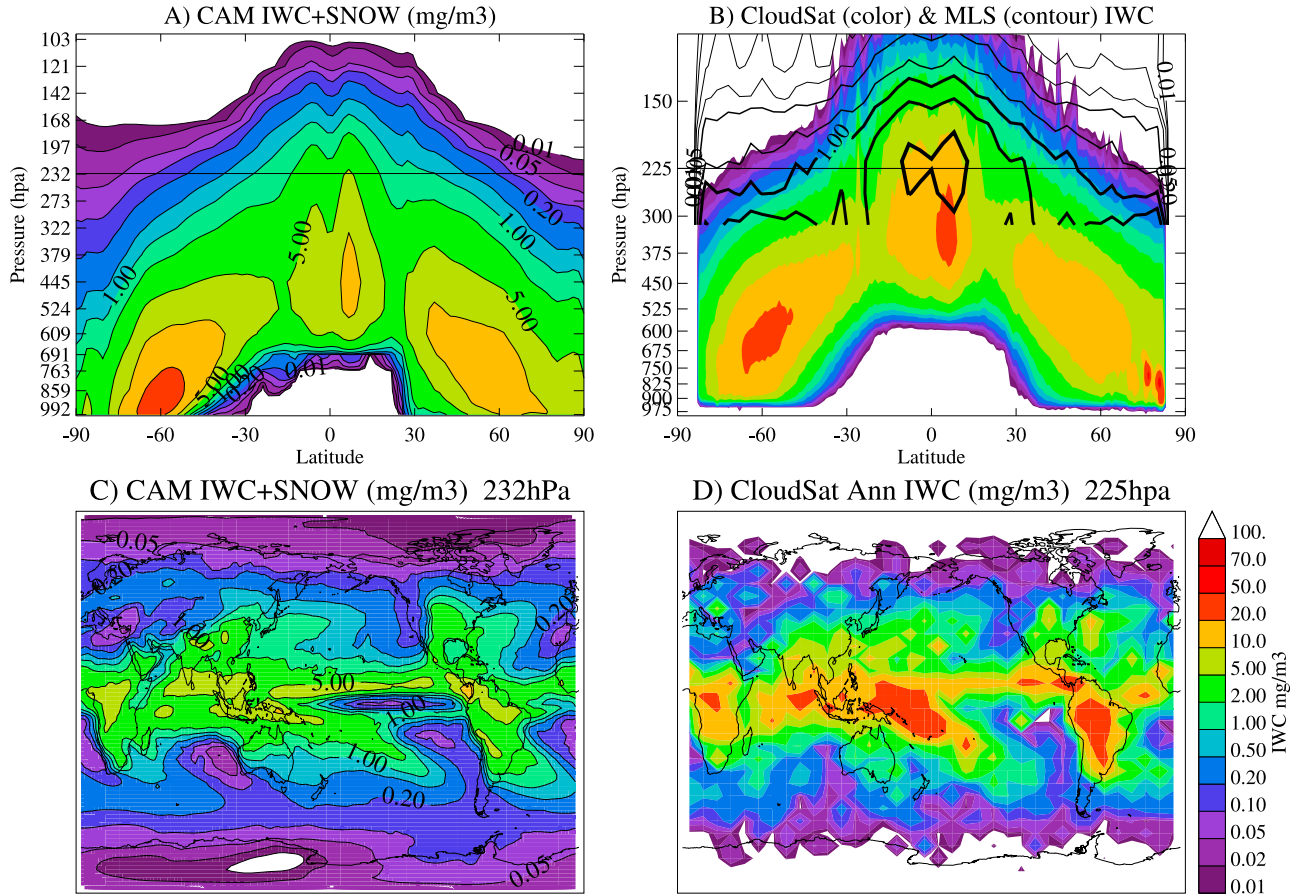


**Figure 4.** (a and b) Zonal mean and (c and d)  $\sim 225$  hPa maps of ice and snow path ( $\text{mg m}^{-3}$ ) from ICE case (Figures 4a and 4c) compared to CloudSat (colored contours) satellite observations (Figures 4b and 4d). Microwave Limb Sounder observations are also shown in Figure 4b (lines) with contour intervals on the same scale.

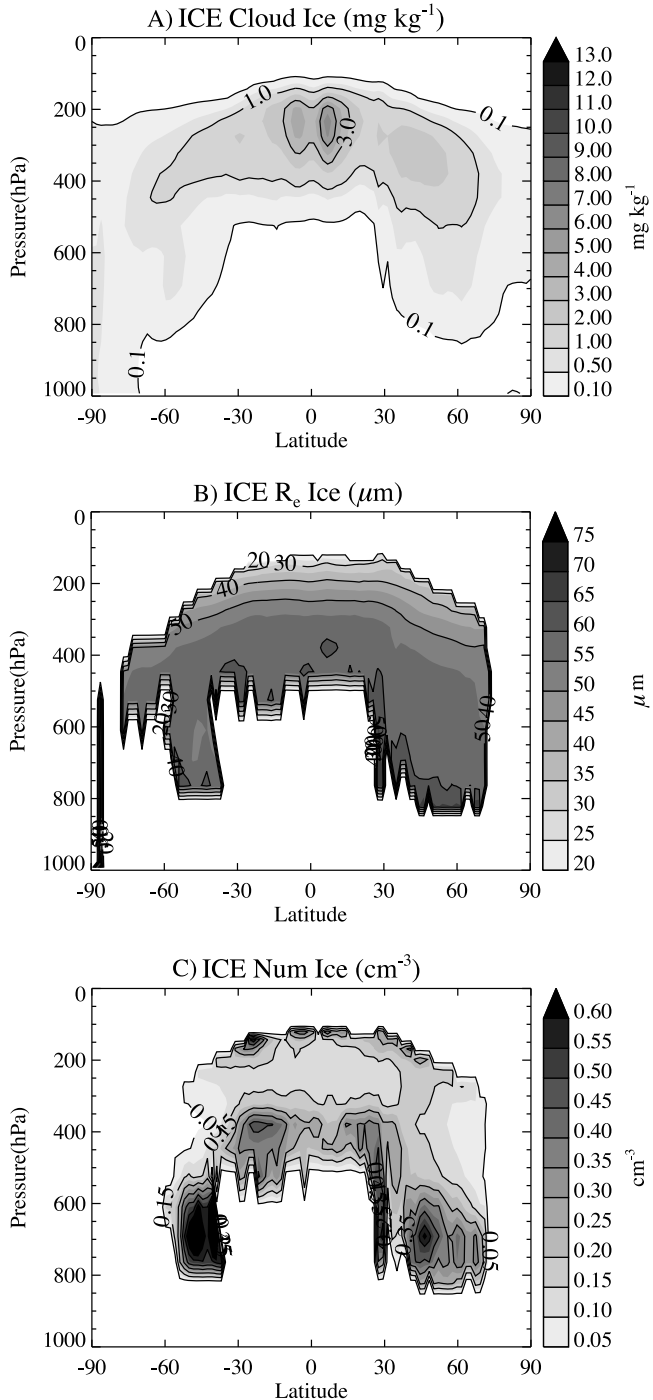


**Figure 5.** Annual zonal mean latitude height plots of (a) cloud ice mass, (b) cloud ice effective radius, and (c) ice number from ICE simulations. Plots have been thresholded by where ice mass is larger than  $0.2 \text{ mg kg}^{-1}$ .

but a reasonable mean mixed phase transition. The ICE simulation is closer to the observations than the CNTL simulation, or the simulations described by Gettelman et al. [2008, Figure 4] using MG2008.

[40] The ice mass, or ice water content (IWC), is an important component of understanding the radiative distribution and impact of high clouds, and has been shown to

vary widely between observations and between observations and models [Waliser et al., 2009]. Differences in retrieved IWC arise due to the sensitivity of instruments to different parts of the ice PSD, and saturation of active and passive sensing wavelengths by ice and liquid. Differences in simulated ice arise from coarse representations of the size distribution and segmentation of ice into up to three species (ice, graupel, and snow) in models (CAM has only two: ice and snow).

[41] Figure 4 compares the mass of ice and snow (total frozen condensate) in the ICE simulation with CloudSat version 5.1 [Waliser et al., 2009] and Microwave Limb Sounder (MLS) [Wu et al., 2009] version 2.2 total IWC satellite retrievals. CloudSat is an active 96 GHz cloud radar with horizontal footprints of 1.3 km cross track, 1.7 km along track and 240 m vertical range. MLS is a microwave limb-viewing instrument with 200 km along track, 7 km cross track and 4 km vertical resolution. Both are in a similar 1330 local equatorial crossing time orbit. Both zonal mean vertical (Figure 4b) and horizontal (Figure 4d) distributions are shown for CloudSat, with the zonal mean MLS IWC measurements as the contour lines in Figure 4b. There are still large uncertainties in the retrieval of IWC from satellites [Waliser et al., 2009]. For example, CloudSat retrievals make assumptions about ice crystal number concentration and cloud phase as a function of temperature. MLS is saturated by thick and dense clouds [Wu et al., 2009].

[42] The simulated IWC distribution peaks in midlatitudes at 800 hPa at  $>20 \text{ mg m}^{-3}$  in Figure 4a, higher in the Southern Hemisphere, in agreement with CloudSat IWC observations (Figure 4b). At midlatitudes in both CAM and CloudSat, ice mass peaks in the storm track regions over the oceans. Overall the ICE simulation seems to have correct ice and snow magnitude at midlatitudes, lower ice and snow mass in the tropical upper troposphere, and slightly lower overall altitudes relative to CloudSat retrievals. The lower altitude may be due to the significant fraction of snow in the ICE simulation (which is averaged in altitude as it falls over the time step). The lower simulated altitude might also be due to the liquid ice partitioning as a function of temperature by CloudSat and the simulation. If model ice occurs at warmer temperatures (Figure 3), or CloudSat prescribed ice at colder temperatures, simulated ice and snow would occur lower in the atmosphere than CloudSat.

[43] In the upper troposphere at  $\sim 225 \text{ hPa}$ , the magnitude of IWC+SNOW in the model (Figure 4c) is less than observed from CloudSat (Figure 4d), mostly because the mass in CAM appears to be shifted lower in altitude. In CloudSat, at least 2/3 of the mass of ice phase species is likely ‘precipitating’. The CAM ICE simulation is similar. The horizontal distribution in the simulations (Figure 4c) reproduces the distribution of the ice phase, but with lower magnitude than CloudSat (Figure 4d).

[44] Figure 5 shows the annual zonal mean of ice mass mixing ratio (not including snow, Figure 5a), ice effective radius (Figure 5b) and ice number concentration (Figure 5c). The ice mass mixing ratio peaks in the tropical upper troposphere near 250–300 hPa at  $3 \text{ mg kg}^{-1}$ . The ice and snow mass peaks slightly lower at  $10 \text{ mg kg}^{-1}$  (Figure 4a). The polar regions and midlatitudes do not have much ice mass (it is mostly snow in Figure 4a). Ice effective radius increases

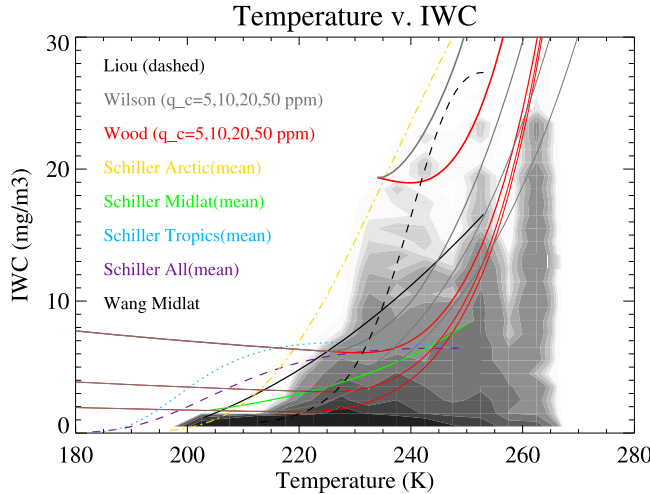


**Figure 6.** In-cloud ice water content (IWC) and in-cloud snow in  $\text{mg m}^{-3}$  as a function of temperature from the ICE run (gray-shaded joint PDF). Data from  $80^{\circ}\text{S}$ – $80^{\circ}\text{N}$  and 500–200 hPa. Snow is added when in-cloud ice mass is greater than 50 ppmm and cloud fraction is greater than 0.05. Various empirical fits to observations shown from Wang and Sassen [2002]: black solid, Liou [1986]: black dashed, Wood and Field [2000]: red, Wilson and Ballard [1999]: gray, and Schiller et al. [2008] for different regions (yellow dash-dotted: Arctic, green solid: midlatitudes, cyan dotted: tropics, and purple dashed: global). Those of Wood and Field [2000] and Wilson and Ballard [1999] are functions of the background water vapor and are shown for 5, 10, 20, and 50 ppmm with thicker lines corresponding to more water vapor. 50 ppmm shown only for  $T > 233\text{ K}$ .

closer to the surface, with higher altitude cirrus clouds having smaller sizes ( $20\text{ }\mu\text{m}$ ) and larger sizes ( $50$ – $60\text{ }\mu\text{m}$ ) found at lower altitudes. Ice number in the region of maximum mass is around  $0.1\text{ cm}^{-3}$  (or  $100\text{ L}^{-1}$ ). Ice nucleation with higher numbers is seen at altitudes above this (pressure  $< 200\text{ hPa}$ ). Ice multiplication (due to shattering of rimed ice crystals) and further nucleation is seen in the mixed phase region (600–800 hPa). At 250 hPa, ice number concentrations are higher over land (typically  $100$ – $300\text{ L}^{-1}$ ), and lower over the oceans and in the Arctic over land ( $20$ – $50\text{ L}^{-1}$ ). Higher concentrations over land appear to be due to more ice nucleation in the simulations, a result of (1) higher turbulence and vertical velocity as well as (2) more heterogeneous nuclei (dust) and sulfate for homogeneous freezing. Note that CloudSat and CAM ice mass peaks over tropical land convective regions (Figures 4c and 4d), but over oceans in midlatitudes.

[45] To explore the ice content in a different way, we compare the in-cloud ice water content in the simulations (including snow) to empirical fits based on observations. The inclusion of snow inside of clouds for in-cloud  $q_i > 0.05\text{ mg kg}^{-1}$  does not substantially alter the PDF (we seek to assess total ice in the cloudy portion of the grid box, not snow without cloud). The fits for comparison are based on in situ observations that do not generally separate precipitation from suspended crystals. Figure 6 compares a joint PDF of IWC as a function of temperature from the ICE simulation with several different empirical formulations from Wang and

Sassen [2002], Schiller et al. [2008], Wood and Field [2000], Wilson and Ballard [1999] and Liou [1986]. All are fits to observations, with those of Wood and Field [2000] and Wilson and Ballard [1999] functions of the background water vapor. The observed variability about the empirical fits is large, and variations between them are also large. Thus these relationships are not a strong constraint on IWC-temperature relationships. The simulations have increasing IWC with temperature as observed, and the peak of the distribution at IWC  $< 7\text{ mg m}^{-3}$  agrees with observations in the 220–250 K temperature range.

[46] Figure 7 illustrates the number of ice particles (including snow in clouds with ice number concentration  $> 1\text{ L}^{-1}$ ) in the ICE simulation as a function of temperature. Instantaneous data up to 120 hPa make up the PDF for all latitudes. Ice concentrations peak between  $30\text{ L}^{-1}$  at 235 K to  $10\text{ L}^{-1}$  at 255K. At colder temperatures ( $T < -35^{\circ}\text{C}$ ), ice nucleation is rapid. Most near surface Arctic points are clustered near 255K and  $10\text{ L}^{-1}$ . The simulated ice crystal concentrations are compared to empirical fits of ice nuclei concentrations in Figure 7. These are not the same quantity, as ice crystal number concentrations can be altered by processes other than nucleation (e.g., depletion by sedimentation or autoconversion, ice multiplication, etc). Gultepe et al. [2001] found average ice crystal concentrations of  $3$ – $10\text{ L}^{-1}$  at temperatures above 230K. The dotted line is from Prenni et al. [2007], a recalculation of Meyers et al. [1992] (solid line) to fit MPACE observations. Also shown are estimates by Cotton et al. [1986] and Fletcher [1962] (on which Cotton et al. [1986] is based). The ice numbers from Cooper [1986] are used by the CNTL and FIXIN case (and fixed at  $220\text{ L}^{-1}$  for  $T < -35^{\circ}\text{C}$  as in MG2008). Values of  $100\text{ L}^{-1}$  seen for CAPT MPACE simulations occur at temperatures from 235–250 K and are largely due to high snow number concentrations.

### 3.3. Ice Nucleation

[47] Ice nucleation in the ICE formulation of the model includes both homogenous freezing of sulfate solution droplets and heterogeneous freezing on dust. Figure 8a shows the fractional contribution of homogenous freezing to total ice crystal formation in the ICE case. At high altitudes and high latitudes of the Southern Hemisphere, homogenous freezing dominates ice nucleation. Note that some of the regions where homogenous freezing dominates are in the stratosphere in polar regions, due to cold temperatures. Not much water is available there for growing nucleated particles, and hence there are not many clouds in these regions of the stratosphere. In the Northern Hemisphere, especially in midlatitudes at levels where significant ice is produced (400–200 hPa), homogenous freezing is about half of the total ice nucleation. A significant fraction of simulated ice nucleation in the ICE run (Figure 8a) is from heterogeneous freezing on dust. In the ICEHI case (Figure 8b), the total number of activated ice nuclei is based on a larger number of sulfate aerosols (homogenous freezing). As a result, in the ICEHI case, ice nucleation (where ice is significant from the surface to 200 hPa in high latitudes and 300–100 hPa in the tropics) is almost entirely dominated by homogenous freezing. In both cases tropical cirrus clouds are dominated by homogenous freezing at pressures less than 150 hPa. This indicates not much dust is present in the upper troposphere, or the conditions are not right for nucleation, and is consistent with

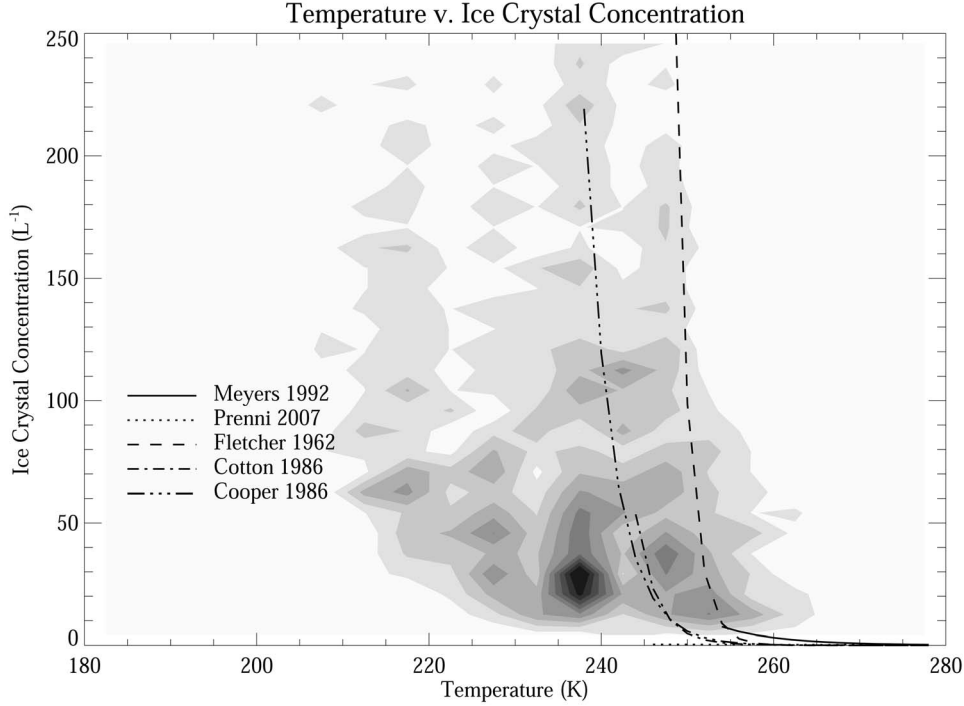


**Figure 7.** Ice number (ice and snow number) as a function of temperature for the ICE case using instantaneous output from 1000 to 120 hPa and all latitudes. Also shown are fits to observations for ice crystal concentrations as a function of temperature based on the study by Fletcher [1962] (dashed) and Cooper [1986] (3-dot dashed). Fits to observations of ice nuclei are shown for the studies by Meyers *et al.* [1992] (solid) and Prenni *et al.* [2007] (dotted), and the parameterization of ice nuclei concentration are from the study by Cotton *et al.* [1986] (dash-dotted).

observed ice nuclei composition, even over land [DeMott *et al.*, 2003a]. However, given significant mineral dust loading, dust dominates ice crystal residuals.

[48] The horizontal distribution of the fraction of homogenous freezing at ice levels (232 hPa) is illustrated in Figure 9 for the ICE case. Heterogeneous nucleation is important in regions over and downwind of dust producing regions, especially the Sahara desert and S. Africa, Australia, and the Gobi desert over central Asia and the N. Pacific. The simulation predicts significant heterogeneous ice nucleation on

dust throughout the Arctic and the N. Hemisphere, while the S. Hemisphere is dominated by homogenous freezing. Note that observations [Quinn *et al.*, 2007] do suggest dust transport into the Arctic is a component of Arctic haze (aerosols).

### 3.4. Supersaturation

[49] The immediate prerequisite for ice nucleation is ice supersaturation [Kärcher and Lohmann, 2002; Kärcher and Haag, 2004]. When ice supersaturation reaches a threshold between water and ice saturation [Koop *et al.*, 2000] or a

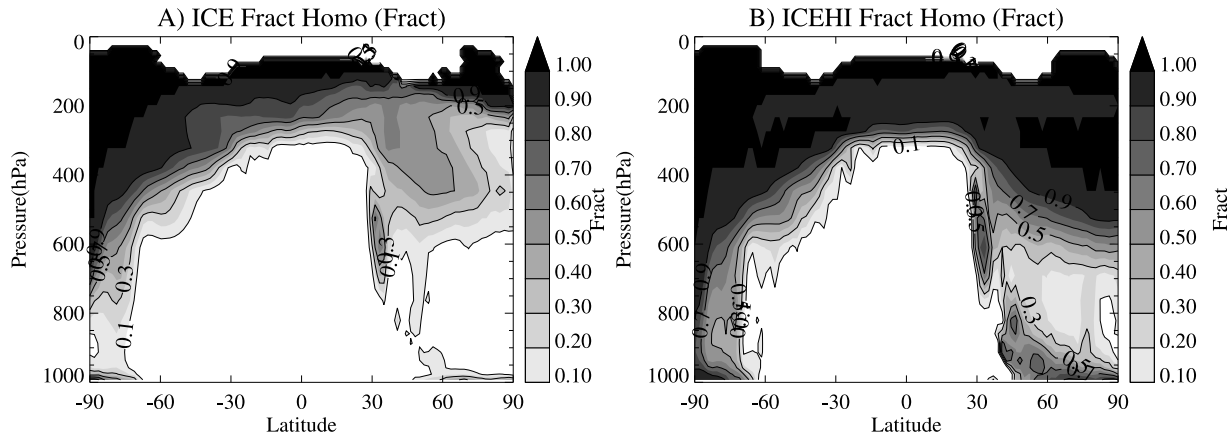


**Figure 8.** Zonal mean fractional contribution to ice crystal number from homogenous freezing from (a) ICE and (b) ICEHI experiments.

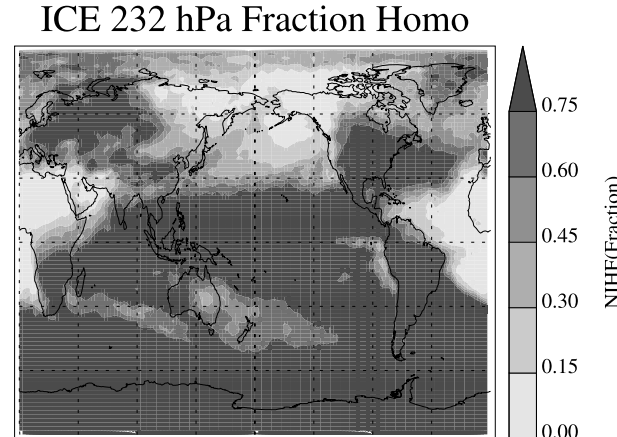


**Figure 9.** Map of the fractional contribution to ice crystal number from homogenous freezing from the ICE experiment at 232 hPa.

threshold sufficient to activate heterogeneous ice nuclei, ice nucleation occurs. Thus representing the distribution of supersaturation is both a driver of and an effect of ice nucleation. Humidity observations in the upper troposphere from the Atmospheric Infra Red Sounder (AIRS) satellite [Gettelman et al., 2006a] and the Measurements of ozone, water vapor, carbon monoxide and nitrogen oxides by Airbus in-service aircraft (MOZAIC) project [Gierens et al., 1999] indicate an exponential decrease in the probability of occurrence of ice supersaturation as humidity gets higher, and rare instances of humidities approaching water saturation. Figure 10 shows a Probability Density Function (PDF)

of relative humidity (RH is calculated over ice and liquid for both observations and the model: ramped between 0°C and -20°C). The region represented (500–200 hPa) has temperatures mostly below -20°C, so this can be thought of as simply RH over ice.

[50] The ICE simulation matches AIRS and MOZAIC observations of ice supersaturation. Both the ICE and CNTL simulations have a high frequency of RH = 100% due to in-cloud points that are not seen in observations due to sampling. The CNTL model has virtually no supersaturation, and the supersaturation is only diagnosed because a combined liquid-ice relative humidity is used in a specified ‘mixed phase’ temperature region (0°C to -20°C). The ICE case has significant supersaturation (global frequency 7.8%). The calculation is performed on instantaneous model output averaged over the meridional and vertical range of MOZAIC aircraft data (from 30°S–60°N and 500–200 hPa). Simulated supersaturation is higher than AIRS (global frequency 1.3%), and lower than MOZAIC (global frequency 18%) observations, but within the range of uncertainty from these two data sources [Gettelman et al., 2006a]. Total frequency is lower. AIRS single profile RH uncertainty is about 20% under ice conditions [Gettelman et al., 2006b].

[51] The simulated zonal mean frequency of supersaturation is compared to AIRS in Figure 11. AIRS water vapor has a minimum threshold of ~20ppmm. No data is available from pressures less than 150 hPa, in the stratosphere, or in regions of deep convection. The general pattern with higher frequencies (of 30%–50%) near the surface at high latitudes and low altitudes, is reproduced by the ICE simulation, with an expected higher frequency than AIRS. As a nadir IR sensor,

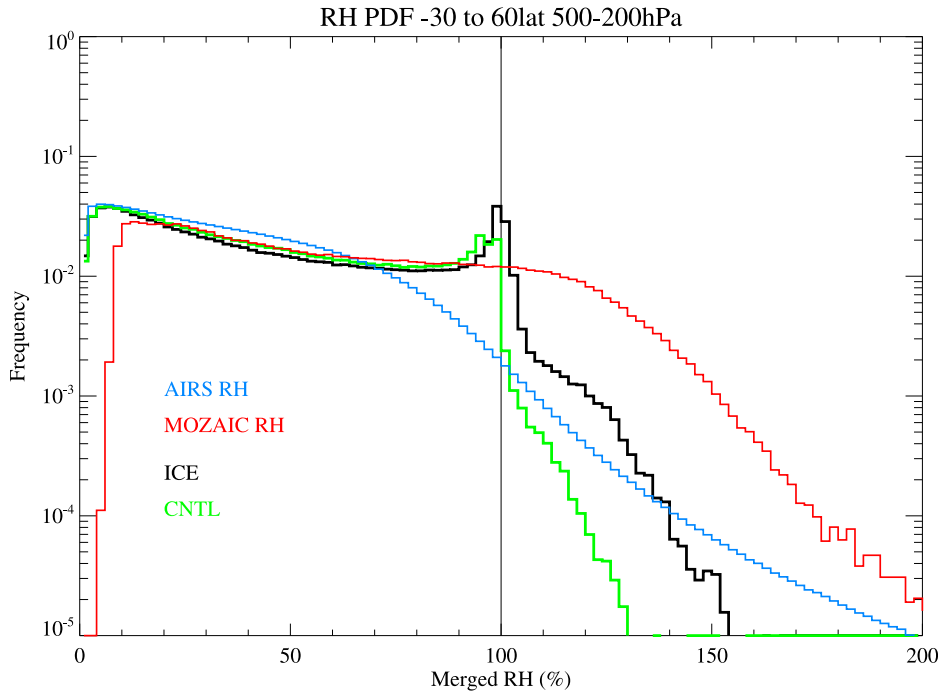


**Figure 10.** Probability distribution function (PDF) of relative humidity (RH) from instantaneous model output from ICE (green) and CNTL (black) simulations, as well as from AIRS (blue) and MOZAIC (red) observations. RH is merged (liquid and ice) RH as described in the text.

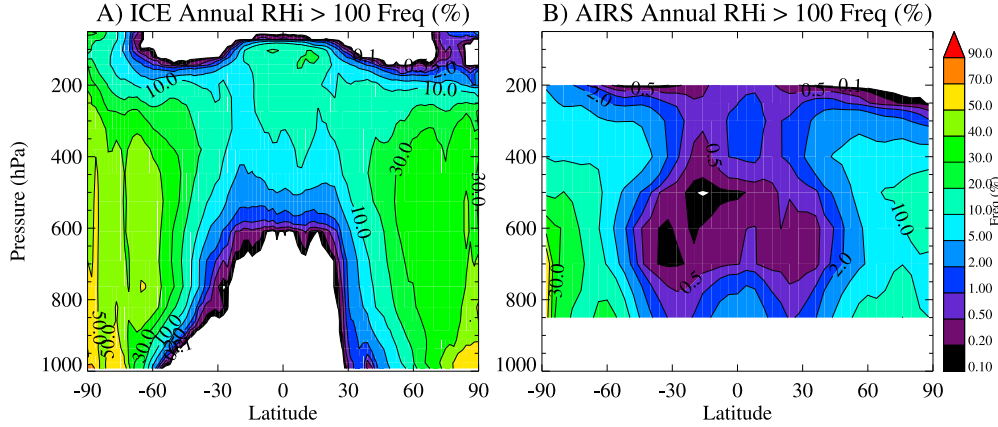


**Figure 11.** Zonal mean annual frequency of ice supersaturation ( $\text{RH} > 100\%$  from (a) ICE simulation and (b) AIRS observations [Gettelman *et al.*, 2006a].

AIRS cannot see the most humid columns within or adjacent to clouds, and so there is an expected dry bias to the AIRS all sky observations, and hence a lower frequency of supersaturation.

[52] Both AIRS and the ICE simulation have a higher frequency of ice supersaturation in the Southern than Northern hemisphere middle and high latitudes (Figure 11). *Ovarlez et al.* [2002] attribute this to differences in aerosol populations, while *Gettelman et al.* [2006a] note that this could be simply due to different temperature variance. *Kahn et al.* [2009] did not see hemispheric differences in temperature variance however.

#### 4. Sensitivity

[53] Here we examine the effect of perturbations to key parameters on the overall climate simulation. The cases are noted in Table 2.

[54] Figure 12 illustrates the different configurations. Cloud top is defined as the first vertical layer with ice or liquid and a cloud fraction of more than 0.05. For comparison with observations, we draw on several sources, including radiative fluxes from the Clouds and the Earth's Radiant Energy System (CERES) algorithms [Wielicki *et al.*, 1996], CloudSat and CALIPSO cloud fractions, and the Advanced Very High Resolution Radiometer (AVHRR) [Han *et al.*, 1998] for cloud microphysics and liquid water path (LWP). Global means are illustrated in Table 3. Common biases are toward a larger net Cloud Radiative Forcing (CRF) than observed due to a longwave clear sky bias (which reduces the longwave cloud forcing), reduced total cloudiness with respect to CloudSat and CALIPSO, and reduced liquid water path compared to satellites. The global mean cloud top liquid particle sizes (CTRe<sub>t</sub>) are smaller than observed by AVHRR.

[55] Broadly, the CNTL case with fixed ice nucleation has cloud top ice numbers between 80 and 100 L<sup>-1</sup> (Figure 12d), relatively small ( $\sim 20 \mu\text{m}$ ) cloud-top ice particles (Figure 12f), lower midlatitude liquid and ice water path (Figures 12g and 12h), cloud drop number (Figure 12c) and total cloud cover (Figure 12b) than observed. The total cloud forcing at mid-latitudes (Figure 12a) is lower than observed, but higher in the tropics. The ICE and ICEHI runs have higher midlatitude

cloud forcing (Figure 12a) that compares better to CERES and higher total cloud cover (Figure 12b) that compares better to CloudSat/CALIPSO. Tropical cloud forcing is slightly lower than the CNTL, in marginally better agreement with observations. Liquid and ice water paths are higher than CNTL. The biggest differences are in the ice number and size: ICEHI (following its name) has high ( $100\text{--}200 \text{ L}^{-1}$ ) ice number at cloud top in the tropics and Northern Hemisphere midlatitudes, and corresponding small ( $<20 \mu\text{m}$ ) ice effective radii in the tropics, whereas the ICE simulation has much lower ( $10\text{--}40 \text{ L}^{-1}$ ) cloud top ice number and larger ( $40 \mu\text{m}$ ) midlatitude and tropical ( $30 \mu\text{m}$ ) ice effective radii where most of the ice mass is located (in the tropics). The ICE simulation values agree better with recent shattering-corrected in situ observations of ice crystal concentration [Jensen *et al.*, 2009; Heymsfield, 2007]. High concentrations in ICEHI result from higher sulfate numbers used for homogenous freezing in the [Liu *et al.*, 2007] parameterization. This result differs from Kay and Wood [2008] who found little sensitivity to aerosol number for the  $w_{\text{sub}}$  in idealized parcel model experiments. The differences are likely due to the very large increase (a factor of 5) in sulfate number used for homogenous freezing and the relatively large  $w_{\text{sub}}$  ( $w_{\text{sub}} > 0.2 \text{ ms}^{-1}$ ).

[56] In addition, we take the ICE experiment and fix ice nucleation as a function of temperature following Cooper [1986], as described by MG2008. The fixed ice nucleation is seen most readily in cloud top ice number (Figure 12d: compare ICE to FIXIN). Since nucleation is fixed by temperature, and set constant for  $T < -35^\circ\text{C}$  (Figure 7), cloud top ice number remains high in the simulations. Ice crystal nucleation in FIXIN does not respond to variations in aerosol loading. The high and constant ice number results in smaller ice effective radii (Figure 12f) and higher ice number concentrations (Figure 12d) that do not agree with observations.

[57] In Figure 13 the ICE case is perturbed by changes to parameters noted in the 'Sensitivity Tests' in Table 2. The auto conversion size threshold (DCS) controls what diameter ice particles are converted to precipitation (MG2008, equation 29). A smaller threshold for DCS (150  $\mu\text{m}$  diameter in the DCS case, from 250  $\mu\text{m}$  in the ICE run) results in more efficient removal of large ice crystals, and thus the remaining ice mass has smaller particles (Figure 13f), and up to 20% lower ice water path (Figure 13h). Cloud forcing

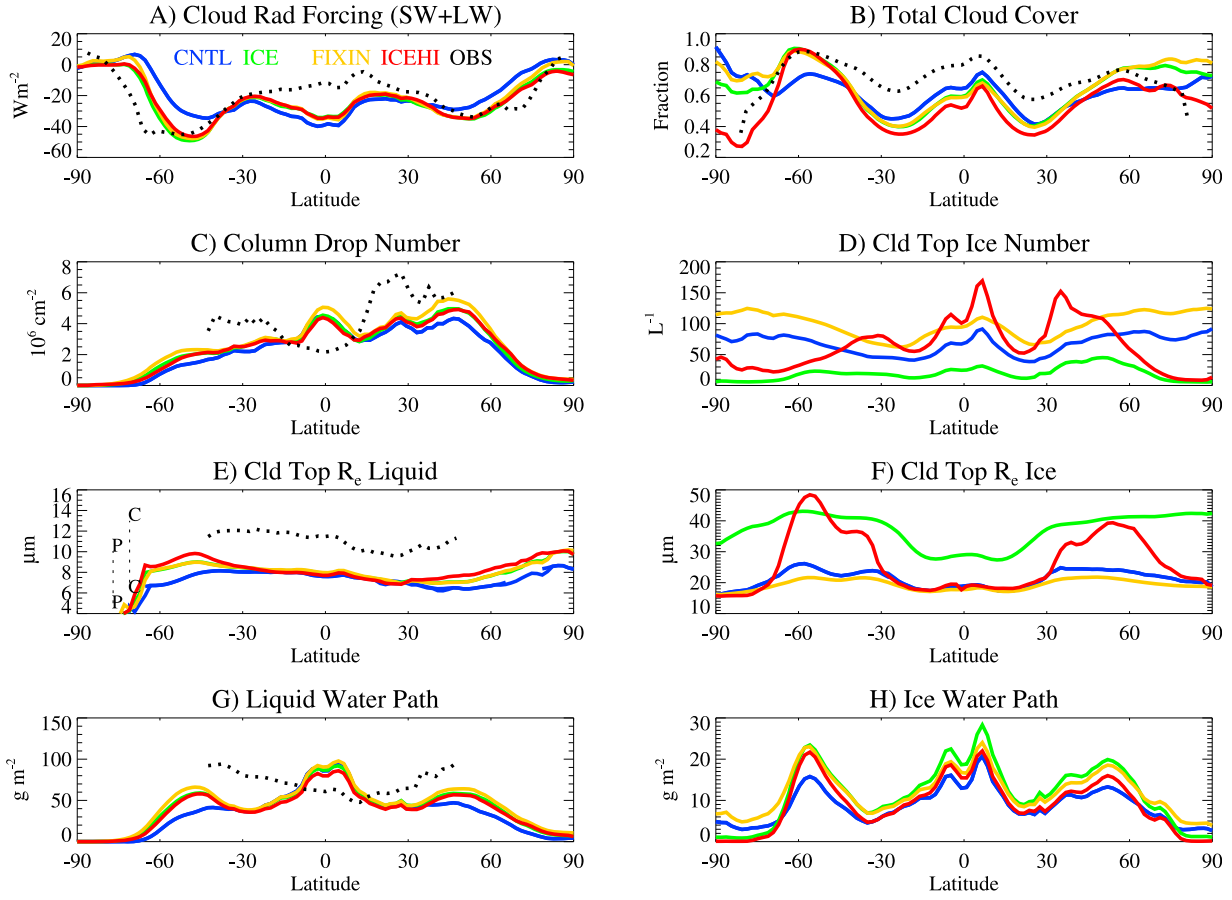


**Figure 12.** Zonal mean distributions of key cloud ice and liquid properties from cases as discussed in the text and in Table 2. CNTL: blue, ICE: green, FIXIN: yellow, ICEHI: red. Observations are shown in black. (a) Net cloud radiative forcing compared to CERES observations. (b) Total cloud cover compared to CloudSat/CALIPSO. (c) Column cloud drop number compared to AVHRR. (d) Cloud top ice number. (e) Cloud top liquid effective radius compared to AVHRR and range of “C”lean and “P”olluted in situ observations described by Gettelman et al. [2008]. (f) Cloud top ice effective radius. (g) Liquid water path compared to AVHRR. (h) Ice water path. References for observations are described in the text.

(Figure 13a) decreases by up to 10% at midlatitudes mostly driven by decreases in longwave cloud forcing. In the NUCALL simulation, temperature-dependent thresholds for initiating ice nucleation are removed, allowing homogenous freezing and heterogeneous nucleation to potentially interact at all temperatures below  $-35^{\circ}\text{C}$ , instead of limiting heterogeneous freezing by a temperature and aerosol number threshold following Liu et al. [2007], equation (10) (dust only). There is little difference from the ICE case, thus the parameterizations for heterogeneous and homogenous freezing are mostly governed by their temperature-dependent process rates (as desired).

[58] In the ICLDF case, the ice cloud fraction ( $CF_i$ ) is modified to fit an empirical formula for in-cloud IWC (ICIWC) as a function of temperature from Wang and Sassen [2002], illustrated in Figure 6. If ice mass mixing ratio ( $q_i$ ) and temperature (T) are prognostic, and  $\text{ICIWC} = f(T)$  then a specified ICIWC provides a diagnostic ice cloud fraction ( $CF_i = q_i/\text{ICIWC}(T)$ ). The result is a 25%–40% (relative) reduction in cloud fraction from the ICE case (Figure 13b). This does not change the net cloud forcing (Figure 13a), but decreases the magnitude of the longwave

**Table 3.** Global Annual Mean Values From Various Runs<sup>a</sup>

Simulation	CNTL	ICE	FIXIN	ICEHI	OBS
CRF ( $\text{W m}^{-2}$ )	-25.6	-27.5	-26.6	-26.8	-17.2 to -23.8
$\text{Cld}_{\text{tot}} (\%)$	59	60	60	53	71
CDNUMC ( $10^6 \text{ cm}^{-2}$ )	2.75	3.04	3.34	3.00	4.01
$\text{CTN}_i (\text{L}^{-1})$	62	22.	91	79.	
$\text{CTRe}_i (\mu\text{m})$	7.2	7.8	7.8	7.9	10.5
$\text{CTRe}_i (\mu\text{m})$	21.1	35.6	19.4	26.3	
LWP ( $\text{g m}^{-2}$ )	46	51	54	48	64 to 155
IWP ( $\text{g m}^{-2}$ )	10	14	13	11	

<sup>a</sup> Shown are total (shortwave + longwave) cloud radiative forcing (CRF) compared to CERES and ERBE observations. Total cloud fraction ( $\text{Cld}_{\text{tot}}$ ) compared to combined CloudSat and CALIPSO retrievals. Grid-mean cloud drop number concentration (CDNUMC) compared to AVHRR data. Cloud top ice number concentration ( $\text{CTN}_i$ ). Cloud top effective radii for liquid ( $\text{CTRe}_i$ ), and ice ( $\text{CTRe}_i$ ) compared to AVHRR observations (liquid only). Grid-mean ice water path (IWP) and grid-mean LWP compared to Moderate Resolution Imaging Spectroradiometer and AVHRR data for liquid.

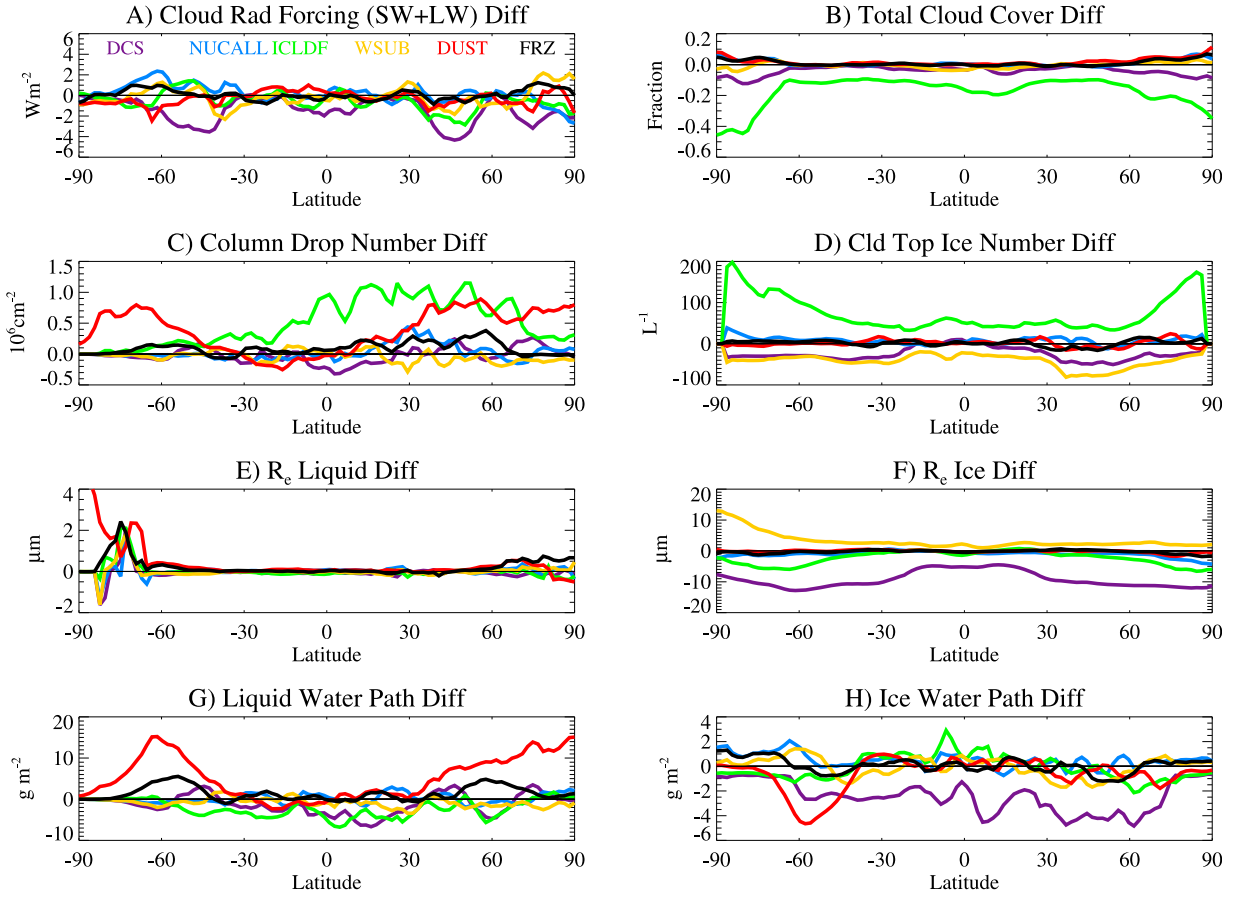


**Figure 13.** Zonal mean distributions of key cloud ice and liquid properties differentiated from the ICE case for cases as discussed in the text and in Table 2. DCS: purple, NUCALL: blue, ICLDF: green, WSUB: yellow, DUST: red, FRZ: black. (a) Cloud radiative forcing. (b) Total cloud cover. (c) Column cloud drop number. (d) Cloud top ice number. (e) Cloud top liquid effective radius. (f) Cloud top ice effective radius. (g) Liquid water path. (h) Ice water path.

and shortwave components by 5–10  $\text{W m}^{-2}$ , a significant degradation with respect to observations (the gross cloud forcing is too low).

[59] In the WSUB case, we significantly reduce the subgrid vertical velocity going into the ice nucleation scheme: from a minimum of  $0.2 \text{ m s}^{-1}$  in the ICE case to a maximum of  $0.2 \text{ m s}^{-1}$ . The effect is to decrease ice number concentration (Figure 13d) and increase ice size (Figure 13f) relative to the ICE case. The radiative effects (Figure 13a) are significant at midlatitudes where cloud forcing decreases by 1–3  $\text{W m}^{-2}$  and the global energy balance shifts by  $0.5 \text{ W m}^{-2}$ . In the Arctic there are large changes in the summer radiative budget (see section 5 and Figure 14).

[60] In the FRZ case, where supercooled rain is instantly frozen at  $-40^\circ\text{C}$  (instead of  $-5^\circ\text{C}$  in the base and other cases), despite large impacts on the snow number concentration for MPACE, there is little global effect, even at high latitudes. The impact is limited to transition seasons (spring and fall) at high latitudes and does not show up in global analyses.

[61] Finally, we explore reducing deposition-condensation freezing on dust parameterized using Meyers *et al.* [1992] by scaling it as a function of dust loading (DUST case). A scaling factor  $S$  for the nucleation rate due to deposition-

condensation freezing ( $N_{dcf}$ ) is calculated from the coarse mode dust number ( $n_d$ ), divided by  $N_{d0}$ , where  $N_{d0} = 0.5 \text{ cm}^{-3}$  defined by in situ measurements [DeMott *et al.*, 2003b]. Thus  $S = \frac{n_d}{N_{d0}}$ . Typically,  $S \ll 1$ . The goal is a sensitivity test that reduces the deposition-condensation freezing in low dust cases. Note that  $N_{d0}$  comes from dust plumes and is likely higher than dust concentrations in measurements used to estimate the [Meyers *et al.*, 1992] parameterization. The effect is most important at mid and high latitudes (Figure 13), where the nucleation significantly increases cloud fraction (Figure 13a), LWP (Figure 13g) and cloud drop number (Figure 13c) at high latitudes by less freezing and retention of more supercooled liquid. This occurs by modifying the partitioning between liquid and ice. The increase in LWP for the DUST case is an improvement as LWP is generally low in the simulations. The DUST case also marginally improves the representation of Arctic radiative fluxes as described in section 5 below.

## 5. Energy Balance Impacts

[62] Finally we use these experiments and sensitivity tests to illustrate the most sensitive regions to ice nucleation. Ice

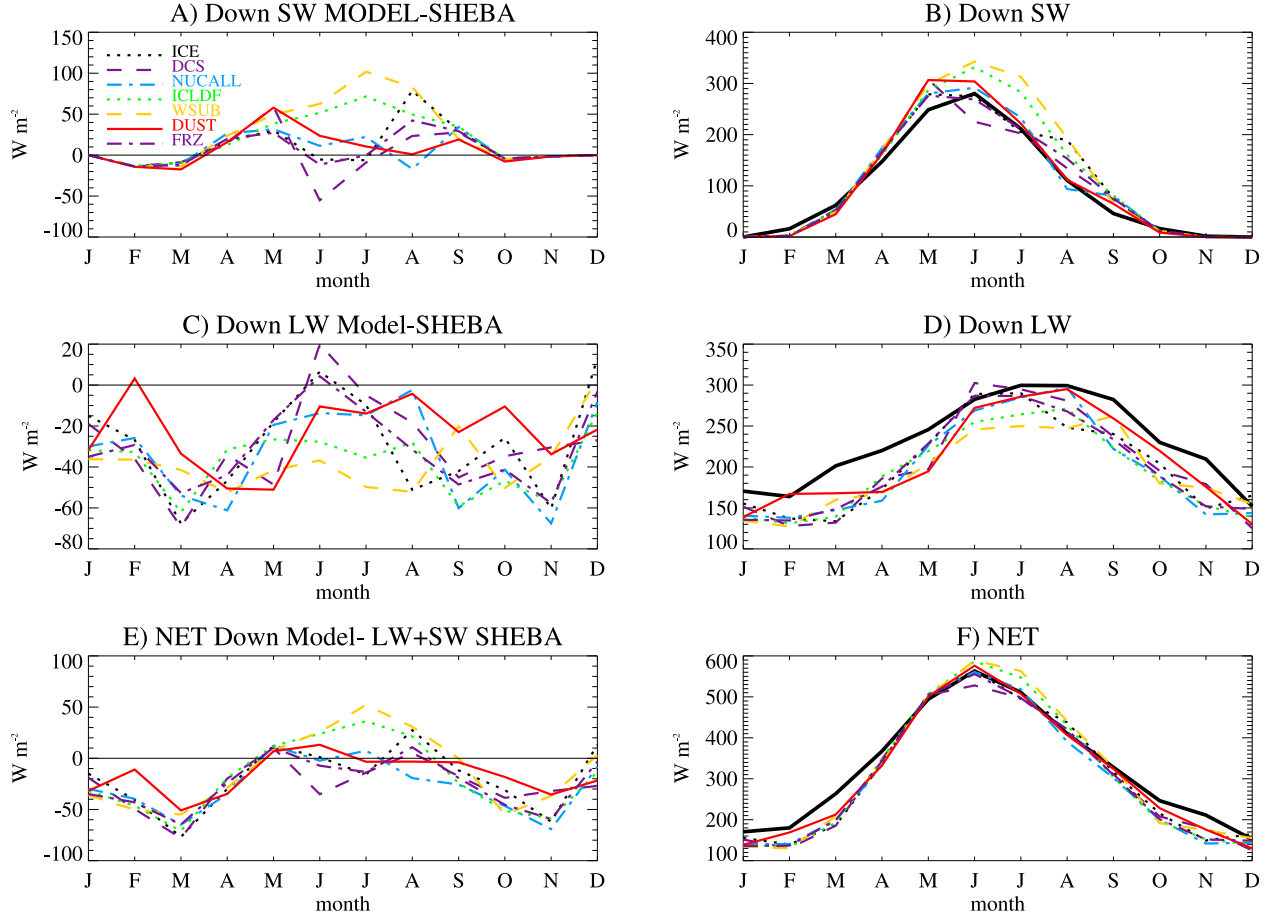


**Figure 14.** Monthly mean surface radiative fluxes over the location of the Arctic SHEBA project ( $77^{\circ}\text{N}$  latitude,  $202^{\circ}$  longitude). Differences from SHEBA observations for (a) downward shortwave (SW) radiation, (c) downward longwave (LW) radiation, and (e) net (LW + SW) radiation. Comparison between SHEBA (thick solid black line) and models shown for (b) downward SW, (d) downward LW, and (f) net (LW + SW). Model simulations shown are the ICE case, and sensitivity experiments are shown in Figure 13 and Table 2.

nucleation primarily affects high latitudes throughout the depth of the troposphere, and the tropics.

[63] High latitudes, especially the Arctic, are particularly sensitive to ice nucleation and mixed phase cloud processes, as noted by Prenni *et al.* [2007]. Cloud cover may change dramatically in the mixed phase regime, critical in the Arctic, as seen in the CAPT experiments (Figure 1). The new parameterization does a significantly better job at reproducing low clouds during MPACE. As is clear from the sensitivity tests and nucleation experiments, there is a significant fraction of heterogeneous freezing on dust that occurs in the Arctic region (Figure 9) and this may cause ice nucleation to vary significantly. In sensitivity tests, changing the deposition-condensation nucleation due to dust or altering the limits on  $w_{\text{sub}}$  (Figure 13) may significantly change the mixed phase, thus altering cloud drop number and liquid water path in the Arctic.

[64] To examine the climate impact of these changes, we compare the surface radiative fluxes in these various simulations to observations during the Surface Heat Budget of the Arctic (SHEBA) field project [Uttal *et al.*, 2002] reported by Intrieri *et al.* [2002]. SHEBA provided observations in the high Arctic over sea ice for an entire annual cycle (Figure 14).

The differences between radiative fluxes between these cases are large, up to  $50 \text{ W m}^{-2}$  for net radiation (Figures 14e and 14f), and larger for individual shortwave and longwave components. The simulations have a bias toward reduced downward longwave radiation and increased downward shortwave radiation relative to SHEBA observations that would seem to imply clouds that are too few or thin. The bias is particularly acute in winter, when there is no shortwave to compensate for the longwave bias. As a result, higher cloud fractions in the DUST simulation are closer to the SHEBA surface balance.

[65] The ICE and DUST cases provide the best representation of the total radiation with DUST marginally better. The observations represent only one location averaged over one year. Slight changes to the ice nucleation and ice parameterization thus may have large effects on the surface radiation balance of the Arctic, which is critical for understanding the evolution of sea ice.

## 6. Discussion and Conclusions

[66] The new ice microphysics parameterization based on Liu *et al.* [2007] has been implemented in the latest version

of the Community Atmosphere Model (CAM). The scheme differs from previous work by putting together state of the art elements and ideas from a variety of previous studies. The parameterization of *Liu et al.* [2007] for ice nucleation is used with an explicit treatment of the mixed phase vapor deposition process (similar to the implicit solution of *Rotstayn et al.* [2000]). Saturation adjustment for ice has been removed for ice clouds as in *Lohmann et al.* [2007], and the ice fraction closure adjusted to permit supersaturation analogous to *Tompkins* [2002], in the context of a two-moment microphysics scheme (MG2008) and a modal aerosol model.

[67] The new scheme provides a better simulation of the mixed phase and ice mass fraction than the older (CNTL) version. The distribution of IWC (ice and snow) is lower than CloudSat in the upper troposphere, but similar in midlatitudes. Simulated IWC is dominated by snow, and is lower in the atmosphere than CloudSat retrievals. IWC as a function of temperature generally agrees with observations, with slightly less ice at warmer (but subzero) temperatures than observed. Ice number concentrations are in reasonable agreement with observations. The model is able to simulate observed large-scale (bulk) supersaturation frequencies and values observed from satellites and aircraft within the large range of uncertainty. The distribution of supersaturation is reasonable: ice supersaturation occurs nearly 30% of the time throughout the depth of the troposphere at high latitudes and in the upper tropical troposphere. The simulations are able to reproduce a hemispheric asymmetry in ice supersaturation, with more in the Southern Hemisphere. CAM provides a useful tool to investigate further the processes responsible for this difference.

[68] Ice crystal formation occurs due to both homogenous freezing and heterogeneous nucleation for mid and high latitude ice clouds. Heterogeneous nucleation is important in the upper troposphere over and downwind of major dust producing regions (Africa, N. East Asia, Australia). Simulated heterogeneous nucleation is active and creates a similar magnitude of crystals to homogenous freezing in the Arctic. Homogeneous freezing dominates in the simulations for cirrus clouds, particularly in the tropics for pressures less than 150 hPa.

[69] The basic ‘ICE’ case has the most realistic cloud forcing and ice number and size of the different schemes examined. The ICEHI case with more active nucleation results in similar climate results, but with much higher number concentrations of small ice particles, which do not agree with most observations when shattering of ice crystals is taken into account. The case with supersaturation and fixed ice nucleation as a function of temperature (FIXIN) creates a more uniform distribution of ice number and size, particularly if supersaturation is also neglected (CNTL). The control case produces cloud forcing that is too small when compared to observations.

[70] The scheme is dependent on several assumptions about subgrid variance of humidity and vertical velocity within a GCM grid cell. There are several parameters representing these processes, including the  $RH_{i\min}$  and  $RH_{i\max}$  for ice cloud fraction, the assumption of RH + 20% for ice nucleation and the estimate of  $w_{sub}$  (see below). The threshold limit on sulfate size (Aitken mode number larger than 0.1  $\mu\text{m}$ ) also is important for ice nucleation. The auto-

conversion of ice to snow, calculated using a size threshold (DCS), strongly affects the total ice water path and the ice particle size remaining in the atmosphere, with a decrease to the size threshold decreasing ice mass and total cloud forcing. The scheme is also sensitive at middle and high latitudes to deposition-condensation freezing on dust (DUST). The scheme is also sensitive to the assumptions about limits on the subgrid vertical velocity (WSUB), with decreasing velocities reducing cloud ice, and cloud forcing over the range of velocities tested (from a minimum of 0.2  $\text{m s}^{-1}$  to a maximum of 0.2  $\text{m s}^{-1}$  and a minimum of 0.001  $\text{m s}^{-1}$ ). Simulations produce similar  $w_{sub}$  to INCA observations in either case due to large scatter of the observations [*Kärcher and Ström*, 2003].

[71] Changing the cloud fraction closure to an empirical fit to observations (ICLDF) also has significant impacts, increasing ice number and reducing ice size and total cloud fraction significantly. It is likely that some of these changes could be reduced by adjusting other parameters (such as the autoconversion size). Changing the freezing temperature of snow (FRZ) reduces snow relative to supercooled rain in the Arctic.

[72] The Arctic region is particularly sensitive to changes to parameters in the ice microphysical scheme. Sensitivity tests indicate large changes to the surface radiative budget in the Arctic as a result of these changes and significant cancellation between longwave and shortwave effects. A correct radiative budget is critical for simulating the balance of Arctic sea ice and its evolution.

[73] Heterogeneous nucleation on dust plays an important role on ice nucleation in the upper troposphere in the simulations. This is especially true in the Arctic, where altering deposition-condensation freezing can significantly perturb clouds. Arctic radiative fluxes are particularly sensitive to ice nucleation. Further work is needed to investigate in more detail the radiative fluxes and role of ice clouds in the Arctic atmosphere, and this new formulation of ice and mixed phase clouds with supersaturation and ice nucleation provides an important tool. A further paper will detail the impact of changing aerosol distributions on ice clouds and climate.

[74] **Acknowledgments.** The National Center for Atmospheric Research is sponsored by the U.S. National Science Foundation (NSF). H. Morrison is partially supported by the NSF Science and Technology Center for MultiScale Modeling of Atmospheric Processes, managed by Colorado State University under cooperative agreement ATM-0425247. Support for S. A. Klein and J. S. Boyle was provided by the Atmospheric Radiation Measurement and Climate Change Prediction Programs of the Office of Science at the U.S. Department of Energy. The contribution of S. A. Klein and J. S. Boyle to this work was performed under the auspices of the U.S. Department of Energy by Lawrence Livermore National Laboratory under contract DE-AC52-07NA27344. Amy Solomon is thanked for providing selected M-PACE cloud property retrieval data. X. Liu and S. J. Ghan were funded by the U.S. Department of Energy, Office of Science, Atmospheric Radiation Measurement, Scientific Discovery through Advanced Computing (SciDAC) program and by the NASA Interdisciplinary Science Program under grant NNX07AI56G. The Pacific Northwest National Laboratory is operated for Department of Energy by Battelle Memorial Institute under contract DE-AC06-76RLO 1830. A. Conley was supported by the SciDAC project from the Department of Energy. We thank J. Kay, S. Massie, and two anonymous reviewers for their comments.

## References

- Ansmann, A., et al. (2008), Influence of Saharan dust on cloud glaciation in southern Morocco during the Saharan Mineral Dust Experiment, *J. Geophys. Res.*, 113, D04210, doi:10.1029/2007JD008785.

- Ansmann, A., M. Tesche, P. Seifert, D. Althausen, R. Engelmann, J. Furntke, U. Wandinger, I. Mattis, and D. Müller (2009), Evolution of the ice phase in tropical altocumulus: SAMUM lidar observations over Cape Verde, *J. Geophys. Res.*, **114**, D17208, doi:10.1029/2008JD011659.
- Bretherton, C. S., and S. Park (2009), A new moist turbulence parameterization in the Community Atmosphere Model, *J. Clim.*, **22**, 3422–3448.
- Clothiaux, E. E., T. P. Ackerman, G. G. Mace, K. P. Moran, R. T. Marchand, M. A. Miller, and B. E. Martner (2000), Objective determination of cloud heights and radar reflectivities using a combination of active remote sensors at the ARM CART sites, *J. Appl. Meteorol.*, **39**, 645–665.
- Collins, W. D., et al. (2004), Description of the NCAR Community Atmosphere Model (CAM3.0), *Tech. Rep. NCAR/TN-464+STR*, Natl. Cent. for Atmos. Res., Boulder, Colo.
- Collins, W. D., et al. (2006), The formulation and atmospheric simulation of the Community Atmosphere Model: CAM3, *J. Clim.*, **19**, 2122–2161.
- Cooper, W. A. (1986), Ice initiation in natural clouds. Precipitation enhancement—A scientific challenge, *Meteorol. Monogr.*, **29**–32.
- Corti, T., B. P. Luo, T. Peter, Q. Fu, and H. Vömel (2005), Mean radiative energy balance and vertical mass fluxes in the equatorial upper troposphere and lower stratosphere, *Geophys. Res. Lett.*, **32**, L06802, doi:10.1029/2004GL021889.
- Cotton, W. R., G. J. Tripoli, R. M. Rauber, and E. A. Mulvihill (1986), Numerical simulation of the effects of varying ice crystal nucleation rates and aggregation processes on orographic snowfall, *J. Appl. Meteorol.*, **16**, 1658–1680.
- DelGenio, A. D., M.-S. Yao, W. Kovari, and K. K.-W. Lo (1996), A prognostic cloud water parameterization for climate models, *J. Clim.*, **9**, 270–304.
- DeMott, P. J., D. J. Cziczo, A. J. Prenni, D. M. Murphy, S. M. Kreidenweis, D. S. Thompson, R. Porys, and D. C. Rogers (2003a), Measurements of the concentration and composition of nuclei for cirrus formation, *Proc. Natl. Acad. Sci.*, **100**, 14,655–14,660.
- DeMott, P. J., K. Sassen, M. R. Poellot, D. Baumgardner, D. C. Rodgers, S. D. Brooks, A. J. Prenni, and S. M. Kreidenweis (2003b), African dust aerosols as atmospheric ice nuclei, *Geophys. Res. Lett.*, **30**(14), 1732, doi:10.1029/2003GL017410.
- Easter, R. C., et al. (2004), MIRAGE: Model description and evaluation of aerosols and trace gases, *J. Geophys. Res.*, **109**, D20210, doi:10.1029/2004JD004571.
- Field, P. R., O. Möhler, P. Connolly, M. Krmer, R. Cotton, A. J. Heymsfield, H. Saathoff, and M. Schnaiter (2006), Some ice nucleation characteristics of Asian and Saharan desert dust, *Atmos. Chem. Phys.*, **6**, 2991–3006.
- Field, P. R., A. J. Heymsfield, and A. Bansemer (2007), Shattering and particle interarrival times measured by optical array probes in ice clouds, *J. Atmos. Oceanic Technol.*, **23**, 1357–1371.
- Fletcher, N. H. (1962), *Physics of Rain Clouds*, Cambridge Univ. Press, New York.
- Gayet, J. F., J. Ovarlez, V. Shcherbakov, J. Strom, U. Schumann, A. Minikin, F. Auriol, A. Petzold, and M. Monier (2004), Cirrus cloud microphysical and optical properties at southern and northern midlatitudes during the INCA experiment, *J. Geophys. Res.*, **109**, D20206, doi:10.1029/2004JD004803.
- Gettelman, A., and D. E. Kinnison (2007), The impact of supersaturation in a coupled chemistry-climate model, *Atmos. Chem. Phys.*, **6**, 1629–1643.
- Gettelman, A., W. J. Randel, F. Wu, and S. T. Massie (2002), Transport of water vapor in the tropical tropopause layer, *Geophys. Res. Lett.*, **29**(1), 1009, doi:10.1029/2001GL013818.
- Gettelman, A., E. J. Fetzer, F. W. Irion, and A. Eldering (2006a), The global distribution of supersaturation in the upper troposphere, *J. Clim.*, **19**, 6089–6103.
- Gettelman, A., V. P. Walden, L. M. Miloshevich, W. L. Roth, and B. Halter (2006b), Relative humidity over Antarctica from radiosondes, satellites and a General Circulation Model, *J. Geophys. Res.*, **111**, D09S13, doi:10.1029/2005JD006636.
- Gettelman, A., H. Morrison, and S. J. Ghan (2008), A new two-moment bulk stratiform cloud microphysics scheme in the NCAR Community Atmosphere Model (CAM3), Part II: Single-column and global results, *J. Clim.*, **21**, 3660–3679.
- Gierens, K., U. Schumann, M. Helten, H. Smit, and A. Marenco (1999), A distribution law for relative humidity in the upper troposphere and lower stratosphere derived from three years of MOZAIC measurements in the upper troposphere and lower stratosphere, *Ann. Geophys.*, **17**, 1218–1226.
- Gultepe, I., G. A. Isaac, and S. G. Cober (2001), Ice crystal number concentration versus temperature for climate studies, *Int. J. Clim.*, **21**, 1281–1302.
- Han, Q., W. B. Rossow, J. Chou, and R. W. Welch (1998), Global survey of the relationships of cloud albedo and liquid water path with droplet size using ISCCP, *J. Clim.*, **11**, 1516–1528.
- Heymsfield, A. J. (2007), On measurements of small ice particles in clouds, *Geophys. Res. Lett.*, **34**, L23812, doi:10.1029/2007GL030951.
- Hoose, C., and J. E. Kristjansson (2010), A classical theory-based parameterization of heterogeneous ice nucleation by mineral dust, soot and biological particles in a global climate model, *J. Atmos. Sci.*, in press.
- Iacono, M. J., J. Delamere, E. Mlawer, M. Shepherd, S. Clough, and W. Collins (2008), Radiative forcing by long-lived greenhouse gases: Calculations with the AER radiative transfer models, *J. Geophys. Res.*, **113**, D13103, doi:10.1029/2008JD009944.
- Intrieri, J. M., C. W. Fairall, M. D. Shupe, P. O. G. Persson, E. L. Andreas, P. S. Guest, and R. E. Moritz (2002), An annual cycle of arctic surface cloud forcing at SHEBA, *J. Geophys. Res.*, **107**(C10), 8030, doi:10.1029/2000JC000423.
- Jensen, E. J., et al. (2009), On the importance of small ice crystals in trop-ical anvil cirrus, *Atmos. Chem. Phys.*, **9**, 5519–5537.
- Kahn, B. H., A. Gettelman, E. J. Fetzer, A. Eldering, and C. K. Liang (2009), Cloudy and clear-sky relative humidity in the upper troposphere observed by the A-train, *J. Geophys. Res.*, **114**, D00H02, doi:10.1029/2009JD011738.
- Kärcher, B., and U. Burkhardt (2008), A cirrus cloud scheme for general circulation models, *Q. J. R. Meteorol. Soc.*, **134**, 1439–1461.
- Kärcher, B., and W. Haag (2004), Factors controlling upper tropospheric relative humidity, *Ann. Geophys.*, **22**, 705–715.
- Kärcher, B., and U. Lohmann (2002), A parameterization of cirrus cloud formation: Homogeneous freezing of supercooled aerosols, *J. Geophys. Res.*, **107**(D2), 4010, doi:10.1029/2001JD000470.
- Kärcher, B., and J. Ström (2003), The roles of dynamical variability and aerosols in cirrus cloud formation, *Atmos. Chem. Phys.*, **3**, 1415–1451.
- Kärcher, B., J. Hendricks, and U. Lohmann (2006), Physically based parameterization of cirrus cloud formation for use in atmospheric models, *J. Geophys. Res.*, **111**, D01205, doi:10.1029/2005JD006219.
- Kärcher, B., O. Möhler, P. J. DeMott, S. Pechtl, and F. Yu (2007), Insights into the role of soot aerosols in cirrus cloud formation, *Atmos. Chem. Phys.*, **7**, 4203–4227.
- Kay, J. E., and A. Gettelman (2009), Cloud influence on and response to seasonal arctic sea ice loss, *J. Geophys. Res.*, **114**, D18204, doi:10.1029/2009JD011773.
- Kay, J. E., and R. Wood (2008), Time scale analysis of aerosol sensitivity during homogeneous freezing and implications for upper tropospheric water vapor budgets, *Geophys. Res. Lett.*, **35**, L10809, doi:10.1029/2007GL032628.
- Klein, S., et al. (2009), Intercomparison of model simulations of mixed-phase clouds observed during the ARM Mixed-Phase Arctic Cloud Experiment. Part I: Single layer cloud, *Q. J. R. Meteorol. Soc.*, **135**, 979–1002.
- Koop, T., B. Luo, A. Tsias, and T. Peter (2000), Water activity as the determinant for homogeneous ice nucleation in aqueous solutions, *Nature*, **406**, 611–614.
- Korolev, A. V., G. A. Isaac, S. G. Cober, J. W. Strapp, and J. Hallett (2003), Microphysical characterization of mixed-phase clouds, *Q. J. R. Meteorol. Soc.*, **129**, 39–65.
- Lawson, R. P., B. Barker, B. Pilson, and Q. Mo (2006), In situ observations of the microphysical properties of wave, cirrus and anvil clouds. Part 2: Cirrus cloud, *J. Atmos. Sci.*, **63**, 3186–3203.
- Liou, K. N. (1986), Influence of cirrus clouds on weather and climate processes: A global perspective, *Mon. Weather Rev.*, **114**, 1167–1199.
- Liu, X., and J. E. Penner (2005), Ice nucleation parameterization for global models, *Meteorol. Z.*, **14**.
- Liu, X., J. E. Penner, S. J. Ghan, and M. Wang (2007), Inclusion of ice microphysics in the NCAR Community Atmosphere Model version 3 (CAM3), *J. Clim.*, **20**, 4526–4547.
- Lohmann, U., P. Stier, C. Hoose, S. Ferrachat, E. Roeckner, and J. Zhang (2007), Cloud microphysics and aerosol indirect effects in the global climate model ECHAM5-HAM, *Atmos. Chem. Phys.*, **7**, 3245–3446.
- McFarquhar, G. M., J. Um, M. Freer, D. Baumgardner, G. L. Kok, and G. Mace (2007a), Importance of small ice crystals to cirrus properties: Observations from the tropical warm pool international cloud experiment (TWP-ICE), *Geophys. Res. Lett.*, **34**, L13803, doi:10.1029/2007GL029865.
- McFarquhar, G. M., G. Zhang, M. R. Poellot, G. Kok, R. McCoy, T. P. Tooman, A. M. Fridlind, and A. J. Heymsfield (2007b), Ice properties of single layer stratocumulus during the Mixed-Phase Arctic Cloud Experiment: 1. Observations, *J. Geophys. Res.*, **112**, D24201, doi:10.1029/2007JD008633.
- Meyers, M. P., P. J. DeMott, and W. R. Cotton (1992), New primary ice nucleation parameterizations in an explicit cloud model, *J. Appl. Meteorol.*, **31**, 708–721.
- Mitchell, D. L. (2000), Parameterization of the Mie extinction and absorption coefficients for water clouds, *J. Atmos. Sci.*, **57**, 1311–1326.

- Mitchell, D. L. (2002), Effective diameter in radiation transfer: General definition, applications and limitations, *J. Atmos. Sci.*, **59**, 2330–2346.
- Mitchell, D. L., A. Macke, and Y. Liu (1996), Modeling cirrus clouds. Part II: Treatment of radiative properties, *J. Atmos. Sci.*, **53**, 2697–2988.
- Mitchell, D. L., A. J. Baran, W. P. Arnott, and C. Schmitt (2006a), Testing and comparing the modified anomalous diffraction approximation, *J. Atmos. Sci.*, **59**, 2330–2346.
- Mitchell, D. L., R. P. d'Entremont, and R. P. Lawson (2006b), Passive thermal retrievals of ice and liquid water path, effective size and optical depth and their dependence on particle and size distribution shape, paper presented at 12th Conference on Atmospheric Radiation, Am. Meteorol. Soc., Madison, Wis.
- Morrison, H., and A. Gettelman (2008), A new two-moment bulk stratiform cloud microphysics scheme in the NCAR Community Atmosphere Model (CAM3), Part I: Description and numerical tests, *J. Clim.*, **21**, 3642–3659.
- Morrison, H., and J. O. Pinto (2005), Mesoscale modeling of springtime arctic mixed-phase stratiform clouds using a new two-moment bulk microphysics scheme, *J. Atmos. Sci.*, **62**, 3683–3704.
- Neale, R. B., J. H. Richter, and M. Jochum (2008), The Impact of Convection on ENSO: From a Delayed Oscillator to a Series of Events, *J. Clim.*, **21**, 5904.
- Nousainen, T., and G. M. McFarquhar (2004), Light scattering by quasi-spherical ice crystals, *J. Atmos. Sci.*, **61**, 2229–2248.
- Ovarlez, J., J. F. Gayet, K. Gierens, J. Strom, H. Ovarlez, F. Auriol, R. Busen, and U. Schumann (2002), Water vapor measurements inside cirrus clouds in northern and southern hemispheres during INCA, *Geophys. Res. Lett.*, **29**(16), 1813, doi:10.1029/2001GL014440.
- Park, S., and C. S. Bretherton (2009), The University of Washington shallow convection and moist turbulence schemes and their impact on climate simulations with the Community Atmosphere Model, *J. Clim.*, **22**, 3449–3469.
- Phillips, T. J., et al. (2004), Evaluating parameterizations in General Circulation Models: Climate simulation meets weather prediction, *Bull. Am. Meteorol. Soc.*, **85**, 1903–1915.
- Prenni, A. J., J. Y. Harrington, M. Tjernstrom, P. J. DeMott, A. Avramov, C. N. Long, S. M. Kreidenweis, P. Q. Olsson, and J. Verlinde (2007), Can ice nucleating aerosols effect Arctic seasonal climate?, *Bull. Am. Meteorol. Soc.*, **88**, 541–550.
- Quinn, P. K., G. Shaw, E. Andrews, E. G. Dutton, T. Ruoho-Airola, and S. L. Gong (2007), Arctic haze: Current trends and knowledge gaps, *Tellus, Ser. B*, **59**, 99–114.
- Roeckner, E., et al. (1996), The atmospheric general circulation model ECHAM4: Model description and simulation of present day climate, *Tech. Rep. 218*, Max Planck Inst. for Meteorol., Hamburg, Germany.
- Rotstayn, L. D., B. F. Ryan, and J. J. Katzfey (2000), A scheme for calculation of the liquid fraction in mixed-phase stratiform clouds in large-scale models, *Mon. Weather Rev.*, **128**, 1070–1088.
- Schiller, C., M. Krämer, A. Afchine, and N. Spelten (2008), The ice water content of Arctic, midlatitude and tropical cirrus, *J. Geophys. Res.*, **113**, D24208, doi:10.1029/2008JD010342.
- Shupe, M. D., P. Kollias, P. O. G. Persson, and G. M. McFarquhar (2008), Vertical motions in arctic mixed-phase stratus, *J. Atmos. Sci.*, **65**, 1304–1322.
- Slingo, J. M. (1987), The development and verification of a cloud prediction scheme for the ECMWF model, *Q. J. R. Meteorol. Soc.*, **113**, 899–927.
- Solomon, A., H. Morrison, O. Persson, M. D. Shupe, and J. W. Bao (2009), Investigation of microphysical parameterizations of snow and ice in arctic clouds during M-PACE through model-observation comparisons, *Mon. Weather Rev.*, **137**, 3110–3128.
- Storelvmo, T., J. E. Kristjansson, U. Lohmann, T. Iversen, A. Kirkevag, and O. Seland (2008), Modeling of the Wegener-Bergeron-Findeisen process: Implications for aerosol indirect effects, *Environ. Res. Lett.*, **3**, 45,001–45,010.
- Tompkins, A. M. (2002), A prognostic parameterization for the subgrid-scale variability of water vapor and clouds in large-scale models and its use to diagnose cloud cover, *J. Atmos. Sci.*, **59**, 1917–1942.
- Tompkins, A. M., K. Gierens, and G. Rädel (2007), Ice supersaturation in the ECMWF forecast system, *Q. J. R. Meteorol. Soc.*, **133**, 53–63.
- Uttal, T., et al. (2002), Surface heat budget of the Arctic Ocean, *Bull. Am. Meteorol. Soc.*, **83**, 255–275.
- Verlinde, J., et al. (2007), The Mixed-Phase Arctic Cloud Experiment, *Bull. Am. Meteorol. Soc.*, **88**, 205–221.
- Waliser, D. E., et al. (2009), Cloud ice: A climate model challenge with signs and expectations of progress, *J. Geophys. Res.*, **114**, D00A21, doi:10.1029/2008JD010015.
- Wang, Z., and K. Sassen (2002), Cirrus cloud microphysical property retrieval using lidar and radar measurements. Part II: Midlatitude cirrus microphysical and radiative properties, *J. Atmos. Sci.*, **59**, 2291–2302.
- Wiacek, A., and T. Peter (2009), On the availability of uncoated mineral dust ice nuclei in cold cloud regions, *Geophys. Res. Lett.*, **36**, L17801, doi:10.1029/2009GL039429.
- Wielicki, B. A., B. R. Barkstrom, E. F. Harrison, R. B. L. III, G. L. Smith, and J. E. Cooper (1996), Clouds and the Earth's Radiant Energy System (CERES): An earth observing system experiment, *Bull. Am. Meteorol. Soc.*, **77**, 853–868.
- Wilson, D. R., and S. P. Ballard (1999), A microphysically based precipitation scheme for the UK meteorological office unified model, *Q. J. R. Meteorol. Soc.*, **125**, 1607–1636.
- Wood, R., and P. R. Field (2000), Relationships between total water, condensed water, and cloud fraction in stratiform clouds examined using aircraft data, *J. Atmos. Sci.*, **57**, 1888–1905.
- Wu, D., et al. (2009), Comparisons of global cloud ice from MLS, CloudSat, and correlative data sets, *J. Geophys. Res.*, **114**, D00A24, doi:10.1029/2008JD009946.
- Xie, S., J. Boyle, S. A. Klein, X. Liu, and S. Ghan (2008), Simulations of Arctic mixed-phase clouds in forecasts with CAM3 and AM2 for MPACE, *J. Geophys. Res.*, **113**, D04211, doi:10.1029/2007JD009225.
- Yang, P., H. Wei, H. L. Huang, B. A. Baum, Y. X. Hu, G. W. Kattawar, M. I. Mishchenko, and Q. Fu (2005), Scattering and absorption property database for nonspherical ice particles in the near- through far-infrared spectral region, *Appl. Opt.*, **44**, 5512–5523.
- Young, K. C. (1974), The role of contact nucleation in ice phase initiation of clouds, *J. Atmos. Sci.*, **31**, 768–776.
- Zhang, M., W. Lin, C. S. Bretherton, J. J. Hack, and P. J. Rasch (2003), A modified formulation of fractional stratiform condensation rate in the NCAR Community Atmospheric Model (CAM2), *J. Geophys. Res.*, **108**(D1), 4035, doi:10.1029/2002JD002523.

J. Boyle and S. A. Klein, Lawrence Livermore National Laboratory, Livermore, CA 94551, USA.

A. J. Conley, A. Gettelman, H. Morrison, and S. Park, Atmospheric Chemistry Division, National Center for Atmospheric Research, Boulder, CO 80305, USA. (andrew@ucar.edu)

S. J. Ghan and X. Liu, Pacific Northwest National Laboratory, Richland, WA 99352, USA.

J.-L. F. Li, Jet Propulsion Laboratory, Pasadena, CA 91109, USA.

D. L. Mitchell, Desert Research Institute, Reno, NV 89512, USA.